Available online at www.sciencedirect.com

ScienceDirect

Geochimica et Cosmochimica Acta 124 (2014) 190–222

Geochimica et Cosmochimica Acta

www.elsevier.com/locate/gca

The Paris meteorite, the least altered CM chondrite so far

Roger H. Hewins [a,b,*], Michèle Bourot-Denise [a], Brigitte Zanda [a], Hugues Leroux [c], Jean-Alix Barrat [d], Munir Humayun [e], Christa Göpel [f], Richard C. Greenwood [g], Ian A. Franchi [g], Sylvain Pont [a], Jean-Pierre Lorand [h], Cécile Cournède [i] Jérôme Gattacceca [i,j], Pierre Rochette [i], Maïa Kuga [k], Yves Marrocchi [k] Bernard Marty [k]

[a] *Laboratoire de Minéralogie et Cosmochimie du Muséum, MNHN and CNRS UMR 7202, 75005 Paris, France*
[b] *Department of Earth and Planetary Sciences, Rutgers University, Piscataway, NJ 08854, USA*
[c] *Unité Matériaux et Transformations, Université Lille 1 and CNRS, UMR 8207, F-59655 Villeneuve d'Ascq, France*
[d] *Université Européenne de Bretagne and CNRS UMR 6538, U.B.O-I.U.E.M., 29280 Plouzané Cedex, France*
[e] *Department of Earth, Ocean and Atmospheric Science and National High Magnetic Field Laboratory, Florida State University, Tallahassee, FL 32310, USA*
[f] *Institut de Physique du Globe de Paris, Sorbonne Paris Cité, Université Paris Diderot, UMR 7154 CNRS, F-75005 Paris, France*
[g] *PSS, Open University, Walton Hall, Milton Keynes MK7 6AA, UK*
[h] *Laboratoire de Planétologie et Géodynamique LPG Nantes – UMR CNRS 6112, 44322 Nantes Cedex 3, France*
[i] *CNRS/Aix-Marseille Université, CEREGE UM34, 13545 Aix-en-Provence, France*
[j] *Department of Earth, Atmospheric, and Planetary Sciences, Massachusetts Institute of Technology, Cambridge, MA 02139, USA*
[k] *Université Lorraine and CNRS, CRPG, UPR 2300, Vandoeuvre les Nancy F-54501, France*

Received 13 February 2013; accepted in revised form 14 September 2013; Available online 8 October 2013

Abstract

The Paris chondrite provides an excellent opportunity to study CM chondrules and refractory inclusions in a more pristine state than currently possible from other CMs, and to investigate the earliest stages of aqueous alteration captured within a single CM bulk composition. It was found in the effects of a former colonial mining engineer and may have been an observed fall. The texture, mineralogy, petrography, magnetic properties and chemical and isotopic compositions are consistent with classification as a CM2 chondrite. There are ~45 vol.% high-temperature components mainly Type I chondrules (with olivine mostly $Fa_{0-2,}$ mean $Fa_{0.9}$) with granular textures because of low mesostasis abundances. Type II chondrules contain olivine Fa_7 to Fa_{76}. These are dominantly of Type IIA, but there are IIAB and IIB chondrules, II(A)B chondrules with minor highly ferroan olivine, and IIA(C) with augite as the only pyroxene. The refractory inclusions in Paris are amoeboid olivine aggregates (AOAs) and fine-grained spinel-rich Ca–Al-rich inclusions (CAIs). The CAI phases formed in the sequence hibonite, perovskite, grossite, spinel, gehlenite, anorthite, diopside/fassaite and forsterite. The most refractory phases are embedded in spinel, which also occurs as massive nodules. Refractory metal nuggets are found in many CAI and refractory platinum group element abundances (PGE) decrease following the observed condensation sequences of their host phases. Mn–Cr isotope measurements of mineral separates from Paris define a regression line with a slope of $^{53}Mn/^{55}Mn = (5.76 \pm 0.76) \times 10^6$. If we interpret Cr isotopic systematics as dating Paris components, particularly the chondrules, the age is 4566.44 ± 0.66 Myr, which is close to the age of CAI and puts new constraints on the early evolution of the solar system. Eleven individual Paris samples define an O isotope mixing line that passes through CM2 and CO3 falls and indicates that Paris is a very fresh sample, with variation explained by local differences in the extent of alteration. The anhydrous precursor to the CM2s was CO3-like, but the two groups differed in that the CMs accreted a higher proportion of water. Paris has little matrix (~47%, plus 8% fine

* Corresponding author at: Laboratoire de Minéralogie et Cosmochimie du Muséum, MNHN and CNRS UMR 7202, 61 rue Buffon, 75005 Paris, France. Tel.: +33 1 4079 3769; fax: +31 4079 5772.
E-mail address: hewins@rci.rutgers.edu (R.H. Hewins).

0016-7037/$ - see front matter © 2013 Published by Elsevier Ltd.
http://dx.doi.org/10.1016/j.gca.2013.09.014

grained rims) and is less altered than other CM chondrites. Chondrule silicates (except mesostasis), CAI phases, submicron forsterite and amorphous silicate in the matrix are all well preserved in the freshest domains, and there is abundant metal preserved (metal alteration stage 1 of Palmer and Lauretta (2011)). Metal and sulfide compositions and textures correspond to the least heated or equilibrated CM chondrites, Category A of Kimura et al. (2011). The composition of tochilinite–cronstedtite intergrowths gives a PCP index of ~2.9. Cronstedtite is more abundant in the more altered zones whereas in normal highly altered CM chondrites, with petrologic subtype 2.6–2.0 based on the S/SiO_2 and $\sum FeO/SiO_2$ ratios in PCP or tochilinite–cronstedtite intergrowths (Rubin et al., 2007), cronstedtite is destroyed by alteration. The matrix in fresh zones has CI chondritic volatile element abundances, but interactions between matrix and chondrules occurred during alteration, modifying the volatile element abundances in the altered zones. Paris has higher trapped Ne contents, more primitive organic compounds, and more primitive organic material than other CMs. There are gradational contacts between domains of different degree of alteration, on the scale of ~1 cm, but also highly altered clasts, suggesting mainly a water-limited style of alteration, with no significant metamorphic reheating.

1. INTRODUCTION

The recently found Paris meteorite is a 1.3 kg fresh, fusion-crusted stone (Fig. 1a). It was purchased by Jacques Corré in 2001 at an auction in the Hôtel-Drouot in Paris, hidden in a box underneath African statuettes. These were part of the effects of Jean Colonna-Cimera, a senior mining engineer in Africa and SE Asia (between 1940 and 1955) who collected artifacts. The stone was later identified as a meteorite by G. Cornen of the Université de Nantes, acquired by the MNHN Paris, classified and officially named "Paris". It is now numbered NMHN 4029. The black shiny fusion crust, which is seen in BSE to contain vesicles and magnetite dendrites (Fig. 1b) is so fresh as to suggest the possibility that the meteorite was an observed fall. On the basis of its Na/K ratio (see below), it appears that the sample was collected before being exposed to rain (Haack et al., 2012). It was probably presented to M. Colonna-Cimera, because of his mining expertise and administrative responsibilities, soon after its fall.

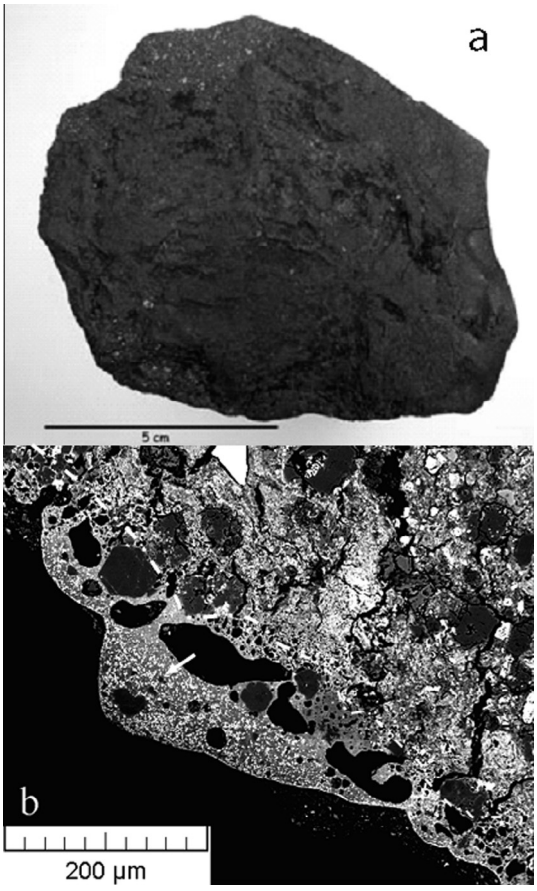

Fig. 1. (a) The 1.3 kg Paris CM chondrite, covered with fresh fusion crust but with the interior exposed at the top. (b) BSE image of the vesicular fusion crust with magnetite dendrites (indicated by white arrow in vesicle) on Paris 2010-1.

Paris was classified as a CM chondrites in 2008 by the second author using petrographic techniques and reported by Bourot-Denise et al. (2010). The classification was confirmed with chemical, oxygen isotopic and chromium isotopic data (Bourot-Denise et al., 2010; Zanda et al., 2010, 2011a,b; Göpel et al., 2011). Here, we present new bulk analyses of Paris and other CM chondrites, for comparison. Paris is heterogeneous, with domains with hydrated minerals much less developed than in other members of this group, though sufficient for classification as CM2, and anhydrous silicates show no effects related to thermal metamorphism, as in type 3.0 chondrites (Bourot-Denise et al., 2010; Zanda et al., 2010, 2011a; Hewins et al., 2011). Though it has experienced aqueous alteration, petrographic and oxygen isotope evidence place it closer to CO chondrites than most other CM chondrites (Bourot-Denise et al., 2010; Zanda et al., 2010, 2011a).

There have been several attempts to devise numerical alteration indices for CM chondrites. The alteration index developed by Browning et al. (1996) was based on the Fe^{3+}/Si ratio in fine matrix, which reflects the replacement of cronstedtite by chrysotile–greenalite solid solution. Rubin et al. (2007) devised a composite index to CM alteration, tracking metal abundance, alteration of chondrule phenocrysts, but in which the composition of PCP (poorly characterized phase) aggregates rather than matrix plays an important role. The petrologic (alteration) subtypes defined range from 2.6 (moderately altered) to 2.0 (totally altered). Rubin et al. (2007) showed that this sequence correlated with decreasing S/SiO_2 and $\Sigma FeO/SiO_2$ in PCP, i.e. the approach to a simple serpentine composition. We attempted to use these composition relations to define the petrologic

subtype of Paris, to see whether the earliest stages of CM alteration fitted into the sequence. Palmer and Lauretta (2011) established an aqueous alteration scale 0–4, based on the replacement by S-rich water of metal grains in matrix or exposed to fluids coming from matrix.

Some CM chondrites are poor in hydrous minerals because of thermal metamorphism (Nakamura, 2005). We used several approaches to search for evidence of reheating – the distribution of Cr in olivine between chromite (Engi, 1983; Johnson and Prinz, 1991) and changes in olivine Cr content due to precipitation of chromite (Grossman and Brearley, 2005). We also studied inclusions containing Si, Cr, P or S in metal, which may be formed during slow chondrule cooling or during metamorphism (Zanda et al., 1994). Finally we examined metal and sulfide compositions and textures, which can indicate the presence and extent of secondary heating (Kimura et al., 2011).

We conclude that Paris has suffered little modification and is the least aqueously altered CM currently known. We present here observations on this exceptional sample, which may contain much well preserved pre-accretionary material not highly susceptible to aqueous alteration and allow us to document the earliest stages of alteration on the CM parent body.

2. SAMPLES AND METHODS

2.1. Polished sections

The Paris meteorite NMHN 4029 was first studied in thin section 2008 LM, and then in parallel polished sections 2010-1 through -9, and 2011-1,-2, using optical microscope, scanning electron microscope (SEM), electron probe microanalyzer (EPMA), and laser ablation inductively coupled plasma mass spectrometry (LA-ICP-MS). A sub-sample called 4029-2.5 was later sectioned. Wavelength-dispersive quantitative analyses of minerals were made on the Cameca SX100 electron microprobe at the Université Paris VI, generally using 15 kV and 10 nA, except for trace elements in olivine, where we used 300 nA beam current. The sections were mapped and textures imaged on a Tescan VEGA II LSU SEM at the LMCM in the Muséum National d'Histoire Naturelle (MNHN) in conventional mode, and minerals were characterized with an SD^3 (Bruker) energy-disperserive spectrometer (EDS) detector. One section was studied by NanoSIMS at the MNHN by Mostefaoui (2011) using a focused Cs^+ ion beam rastered over $9 \times 9\ \mu m^2$ areas. Negative secondary ions of the three O-isotopes, ^{28}Si, and $^{27}Al^{16}O$ were simultaneously measured in multi-collection mode in an unsuccessful search for presolar silicates or oxides. A separate section (SPSR-1) was prepared for Remusat et al. (2011) without using epoxy. This was also studied by NanoSIMS using rastering of a focused Cs^+ beam to generate secondary ion images of H^-, D^-, $^{12}C^-$, $^{16}O^-$, $^{26}CN^-$, $^{28}Si^-$ and $^{32}S^-$.

2.2. TEM sections

Four electron-transparent sections were prepared from SPSR-1 for transmission electron microscopy (TEM) by the focused ion beam (FIB) technique using an FEI Strata DB 235 at the University of Lille (see Zega et al., 2007, for detailed preparation procedure). The FIB sections were extracted from the matrix at different distances from a chondrule. They were examined by TEM with an FEI Tecnai G2-20 TWIN (LaB6, 200 kV) equipped with an energy dispersive spectrometer (EDS) at the University of Lille. Mineralogy was studied using bright field TEM imaging and electron diffraction. Scanning TEM (STEM) was used for acquiring EDS data for microanalysis. Quantitative analyses were obtained with k-factors (experimentally determined) and absorption corrections. Elemental distributions were obtained by EDS X-ray intensity maps, using spectral imaging wherein each pixel of a spectrum image contains a full EDS spectrum (see Leroux et al. (2008) for details).

2.3. Chemical composition

A 13 g sample was crushed using a boron carbide mortar and pestle into a homogenous fine-grained powder in clean room conditions at the Institut Universitaire Européen de la Mer (IUEM), Plouzané. A 500 mg aliquot was dissolved and analyzed for major and trace element concentrations by ICP-AES (inductively coupled plasma – absorption emission spectrometry) using a Horiba Jobin Yvon Ultima 2 spectrometer, and by ICP-SFMS (inductively coupled plasma – sector field mass spectrometry) using a Thermo Element 2 spectrometer following the procedures described by Barrat et al. (2012). The concentration reproducibility is generally much better than 5% at the chondritic level.

Major and trace element concentrations were measured by LA-ICP-MS using a New Wave UP193FX ArF excimer laser system coupled to a Thermo Element XR at the Plasma Analytical Facility at the National High Magnetic Field Laboratory, Florida State University. This involved in-situ rastering with LA-ICP-MS of a 0.25 cm^2 square in a comparatively altered region of section 2010-4. In addition, spot analyses by LA-ICP-MS were used to analyze matrix in the least altered regions as well as in more altered regions resembling more typical CM chondrites. Major aspects of the instrumentation and methodology have been described previously (Humayun et al., 2007, 2010; Gaboardi and Humayun, 2009; Humayun, 2012).

2.4. Oxygen isotopes

High-precision oxygen isotopic measurements were performed at the Open University using an infrared laser-assisted fluorination system (Miller et al., 1999). A total of eleven individual analyses of whole rock chips and powders from Paris were undertaken, with each replicate having a mass of about 2 mg. After fluorination, the O_2 released was purified by passing it through two cryogenic nitrogen traps and over a bed of heated KBr. O_2 was analyzed using a MAT 253 dual inlet mass spectrometer. Analytical precision (1σ), based on replicate analyses of international (NBS-28 quartz, UWG-2 garnet) and internal standards, is approximately $\pm 0.04‰$ for $\delta^{17}O$; $\pm 0.08‰$ for $\delta^{18}O$; $\pm 0.024‰$ for $\Delta^{17}O$ (Miller et al., 1999). Oxygen isotopic analyses are

reported in standard δ notation, where $\delta^{18}O$ has been calculated as: $\delta^{18}O = [(^{18}O/^{16}O_{sample}/^{18}O/^{16}O_{ref.})-1] \times 1000(‰)$ and similarly for $\delta^{17}O$ using the $^{17}O/^{16}O$ ratio. $\Delta^{17}O$, which represents the deviation from the terrestrial fractionation line, has been calculated as: $\Delta^{17}O = \delta^{17}O–0.52\delta^{18}O$ in order to compare our results with those obtained by Clayton and Mayeda (1999).

2.5. Gas analyses

Two fragments of Paris (Paris-A and Paris-B) were analyzed in order to determine their noble gas abundances and isotopic compositions. Each sample was weighted and placed in a hemispherical cavity in a laser chamber developed at the CRPG for the analysis of nitrogen (see Humbert et al., 2000 for details). The chamber was maintained for 48 h at 373 K under vacuum to remove atmospheric contamination. The samples were heated for 1 min with a CO_2 laser beam (wavelength of 10.6 μm) to different temperature steps by increasing the laser power, the last step corresponding to the fusion of the sample (Marty et al., 2010). The released gas was purified using two Ti–Zr getters to remove active gases (10 min at 800 °C, 10 min at room temperature). Analysis of noble gases was performed with a static sector-type mass spectrometer in monocollection mode (Marrocchi et al., 2011). Each sample has been bracketed by two standards for which the amounts of noble gases were adjusted to be comparable to the sample abundance. The blanks determined for laser extraction by heating an empty cavity were less than 0.1% and correspond to (in cm^3) 1.15×10^{-10}, 6.51×10^{-12}, 2.44×10^{-10} and 2.78×10^{-15} for ^4He, ^{20}Ne, ^{40}Ar and ^{130}Xe, respectively.

2.6. Magnetic properties

All magnetic measurements were performed at CEREGE (Aix-en-Provence, France), with the exception of magnetic property measurement system (MPMS) measurements (at IPGP, Paris, France). Magnetic hysteresis measurements were performed with a Princeton Micromag Vibrating Sample Magnetometer with a maximum applied field of 1 T and a sensitivity of $\sim 5 \times 10^{-9}$ Am^2. The analysis of hysteresis loops provided the ratio of saturation remanent magnetization (M_{RS}) to saturation magnetization (M_S) and the coercive force (B_C). High field susceptibility (χ_{HF}) was determined by a linear fit for applied fields >0.9 T of the hysteresis loops. Remanent coercive force (B_{CR}) was determined by DC back field experiments performed with the VSM. We measured the S ratio, defined as the isothermal remanent magnetization (IRM) obtained after applying a 3 T field and then a back field of −0.3 T normalized to the 3 T IRM. Low-temperature remanence measurements were performed with an MPMS from Quantum Design®. This instrument has a moment sensitivity of 10^{-11} Am^2. The low field specific susceptibility (written as χ in m^3/kg) and its evolution with temperature were measured using an Agico MFK1 apparatus with a sensitivity of 5×10^{-13} m^3, operating at 200 A/m and a frequency of 976 Hz, equipped with a CS3 furnace and a CSL cryostat. IRMs were imparted using a pulse magnetizer from Magnetic Measurements. Thermal demagnetization was performed using an MMTD furnace, under argon atmosphere above 250 °C. Remanence measurements were performed with a SQUID cryogenic magnetometer (2G Enterprises, model 755R, with noise level of 10^{-11} Am^2).

2.7. Mg and Cr isotopes

Mineralogical separates were prepared at the IPGP by using the freeze–thaw method and subsequent separation by magnetic susceptibility and by density. Handpicking produced pure magnesian and ferroan olivine from Type I and II chondrules, a separate of fine-grained material attached to chondrules (presumably fine-grained rims). These and an aliquot of the bulk rock from the large IUEM sample were used for Cr isotope analysis by mass spectrometry (Göpel et al., 2011). Metal and sulfide separates were also produced, the latter for S isotope measurements by P. Cartigny. Pure hibonite grains handpicked from these fractions were mounted in epoxy, polished and studied with SEM to identify their mineralogy and morphology. Magnesium isotope measurements were performed on the hibonite with CAMECA 1280HR2 at CRPG (Liu et al., 2012).

3. CLASSIFICATION, ISOTOPES AND CHEMISTRY

Paris is classified as a CM2 chondrite. It consists mainly of Type I chondrules in a matrix containing chrysotile–greenalite–cronstedtite serpentine and PCP (fine-grained cronstedtite–tochilinite intergrowths in highly altered CM chondrites). It has a grain density of 2.92 (Zanda et al., 2010), typical of CM chondrites (Consolmagno et al., 2008). Bulk chemical and O and Cr isotopic data reported below also support a classification for Paris as CM chondrite. We observed no evidence of terrestrial weathering in trace element concentrations, or of shock.

Apparent matrix content has been considered as a measure of the extent of alteration of CM chondrites (McSween, 1979). Preliminary BSE image analyses (Bourot-Denise et al., 2010) showed that Paris has less matrix than Murchison (66% vs. 71%), which McSween (1979) showed to be one of the least matrix-rich, "partially altered" CM falls. We attempted to extend this approach by identifying chondrule fragments in BSE images down to about 100 μm and also by counting fine-grained rims on chondrules separately. Matrix abundance was thus determined to be approximately 47%, with 8% fine grained rims (FGR) and 45% chondrules. Modal analysis showed 57–85% matrix in other CM chondrites (Grossman and Olsen, 1974; McSween, 1979).

3.1. Oxygen isotopes

The results of oxygen isotope measurements of Paris are given in Table 1 and plotted in Fig. 2a and b. The eleven individual analyses of Paris obtained in this study show a wide range of values with respect to $\delta^{17}O$ and $\delta^{18}O$ (Fig. 2a), reflecting the isotopically heterogeneous composition of its constituent components (chondrules, CAIs, crystal fragments, hydrated phases). From an oxygen isotope

Table 1
Oxygen isotope results.

Sample	COMMENTS	$\delta^{17}O‰$	1σ	$\delta^{18}O‰$	1σ	$\Delta^{17}O‰$	1σ
Paris (unaltered)	Less altered lithology	−2.11		2.43		−3.37	
Paris (unaltered)	Less altered lithology	−1.43		4.40		−3.72	
Paris (unaltered)	Less altered lithology	−0.37		6.14		−3.56	
Paris (altered)	More altered lithology	0.33		6.21		−2.91	
Paris (altered)	More altered lithology	0.75		6.80		−2.79	
Paris (chips)	Chips	−1.15		4.09		−3.28	
Paris (chips)	Chips	−1.87		3.63		−3.76	
Paris (chips)	Chips	−2.15		3.44		−3.94	
Paris	Powder	0.62		6.97		−3.00	
Paris	Powder	−0.66		5.11		−3.31	
Paris	Powder	−1.20		4.68		−3.63	
	MEAN ($n = 11$)	−0.84	1.06	4.90	1.48	−3.39	0.39

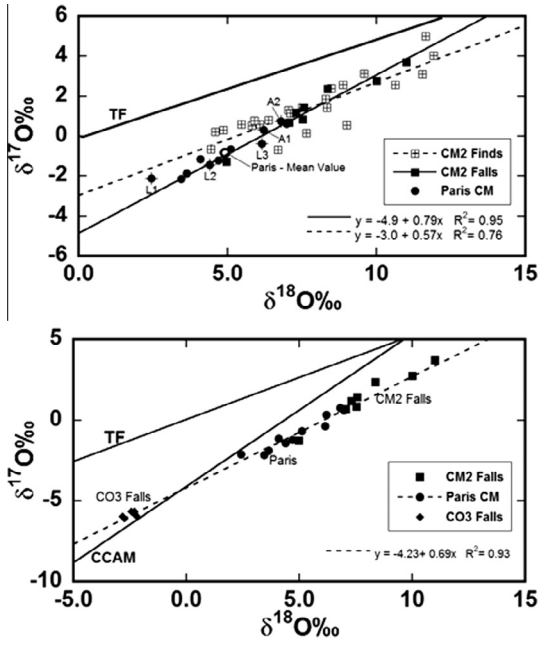

Fig. 2. (a) Oxygen isotope composition of Paris meteorite compared to other CM falls and finds. A1 and A2 are altered lithologies from Paris. L1, L2 and L3 are less altered lithologies from Paris. The mean composition of the Paris meteorite is shown by the open circle. The dashed regression line is fall and finds data from Clayton and Mayeda (1999) only, whereas the solid regression line if for finds and includes the data of Clayton and Mayeda (1999) and the recent CM falls Sayama (Grossman and Zipfel, 2001) and Maribo (Haack et al., 2012). (b) Best fit linear regression line through the oxygen isotope data for Paris samples only. The fact that this regression line passes through the relatively narrow field defined by CO3 chondrites provides strong evidence that both the CM and CO groups are genetically related. CM data: Clayton and Mayeda (1999), Grossman and Zipfel (2001), Haack et al. (2012). CO3 data: Greenwood and Franchi (2004).

perspective, CM2 meteorites are essentially a two component mix between ^{16}O-enriched anhydrous silicates and ^{16}O-depleted hydrated phases (Clayton and Mayeda, 1999). This can clearly be seen in the case of the Paris meteorite, with analyses defining a distinct linear trend with a slope of 0.69 ($R^2 = 0.93$) and an intercept of −4.23‰ (Fig. 2b). In comparison, the combined CM2 fall and find data of Clayton and Mayeda (1999) show significant scatter and define a shallower trend with a slope of 0.57 ($R^2 = 0.76$) and an intercept of −3.0‰ (Fig. 2a).

The CM2 data of Clayton and Mayeda (1999) included a significant number of analyses from Antarctic finds. If CM falls data alone are considered, a much simpler picture emerges. In Fig. 2a we have plotted just the falls data from Clayton and Mayeda (1999), plus analyses of two other recent CM2 falls: Maribo (Haack et al., 2012) and Sayama (Grossman and Zipfel, 2001). CM2 fall data define a linear array that is significantly steeper than the combined CM2 fall and find data, having a slope of 0.79 ($R^2 = 0.95$) and an intercept of −4.9‰ (Fig. 2a). This suggests that the relatively shallow slope of the combined fall and find CM2 dataset obtained by Clayton and Mayeda (1999) is principally a reflection of the very large number of weathered Antarctic finds that it contains. Compared to meteorite falls, weathered Antarctic finds are generally displaced to less negative $\Delta^{17}O$ values, as a result of interaction with terrestrial precipitation (Greenwood and Franchi, 2004; Greenwood et al., 2012). However, unlike other meteorite groups, it is not possible to use leaching techniques on CM2 samples to mitigate the effects of weathering, as such treatment will also remove the indigenous low temperature component.

Clayton and Mayeda (1984, 1999) demonstrated that the anhydrous silicates in CM2s have an oxygen isotopic composition similar to that of CO3 chondrites and suggested that there may be a genetic link between the two groups. The extension of the linear regression line fitted to the Paris data intersects the CO3 field of Greenwood and Franchi (2004) (Fig. 2a). The slope of the Paris regression line is essentially identical in slope to that proposed by Clayton and Mayeda (1999) as being a best fit through their CO and CM whole rocks and CM matrix separates. The fact that the regression line for Paris passes through the relatively narrow field defined by CO3 chondrites provides strong evidence that both the CM and CO groups are genetically related. In addition, analyses from Paris significantly extend the ^{16}O-enriched end of the CM2 trend (Fig. 2a and b); a feature that is consistent with it being less

hydrated than the least hydrated CM fall and having the least matrix abundance of any member of the group so far studied.

In addition to bulk powders from Paris, chips from two distinct lithologies, one altered and one less altered, were analyzed during the course of these study. Analyses from the less altered material are labeled L1 to L3 on Fig. 2a, analyses from the more altered lithology are labeled A1 and A2 on Fig. 2a. The less altered lithology shows a significant spread in oxygen isotope compositions and includes the most ^{16}O-rich material yet analyzed from a CM2 chondrite (point L1). In comparison, the altered lithology appears to have a more uniform ^{16}O-poor composition (Fig 2a).

3.2. Chromium isotopes

The sequential dissolution pattern, a feature distinguishing between the different carbonaceous chondrite classes, is very similar to that of the Murchison CM. The ε^{54}Cr value of the bulk rock, $\varepsilon^{54}Cr = 0.925 \pm 0.094$ (Göpel et al., 2011), falls on the correlation line that has been established between ε^{54}Cr and Δ^{17}O for carbonaceous chondrites (Trinquier et al., 2007). This is shown by Göpel et al. (2012) and is consistent with the classification of Paris as a CM chondrite.

Forsteritic olivine, fayalitic olivine, respectively from Type I and Type II chondrules, a separate of fine-grained material attached to chondrules, presumably in fine-grained rims (FGR) and an aliquot of the bulk rock were analyzed for Mn/Cr systematics (Göpel et al., 2011, 2012). The data are presented in Göpel et al. (2013).

All mineral fractions as well as the bulk rock of Paris exhibit a positive ε^{54}Cr anomaly typical for carbonaceous chondrites. The mineral samples fall on a line with a slope of $^{53}Mn/^{55}Mn = (5.76 \pm 0.76) \times 10^{-6}$ with an initial $^{53}Cr_i = -0.132 \pm 0.055$.

If we interpret these isotopic data of the minerals as providing direct chronological information (the homogeneity of ^{54}Cr in the different materials has especially to be considered), the corresponding age for the Paris components, particularly of Type I and Type II chondrules, is 4566.44 ± 0.66 Myr based on the D'Orbigny anchor (Glavin et al., 2004; Amelin, 2008) recalculated with the U isotopic composition measured by Brennecka and Wadwha (2012).

The Mn–Cr study suggests early formation ages for the Paris chondrules (<1 Myr after CV CAIs and confirms a previous Mn/Cr study on Allende chondrules revealing the antiquity of Allende chondrules (Yin et al., 2007, 2009). Such an old age is also compatible with a more recent U/Pb study on refractory inclusions from CV chondrites (Efremovka and Allende) as well as on individual chondrules from Allende and the unequilibrated OC NWA 5697. These U/Pb isotope data define a short formation interval for the CAIs (4567.30 ± 0.16 Myr), while chondrule ages range from 4567.32 ± 0.42 to 4564.1 ± 0.30 Myr (Connelly et al., 2012). The authors emphasize "these data refute the long-held view of an age gap between CAIs and chondrules and indicate that chondrule formation started contemporaneously with CAIs". Such an early chondrule formation is as yet difficult to reconcile with the accretion age of the CM parent body (~3 Myr after CAIs) and with the Mg/Al isotope data of CO chondrules that systematically formed ~2–2.5 Myr after CAIs (Kita and Ushikubo, 2012; Fujiya et al., 2013).

3.3. Bulk chemistry

Paris, and the CM chondrites Nogoya and Boriskino (2 samples) were analyzed together at UBO. With 32.05 wt.% Fe_2O_3 total, 28.72 wt.% SiO_2, 28.72 wt.% MgO and LOI 12.9 wt.% (Table 2), the aliquot from the 13 g sample of Paris falls well within the ranges for CM chondrites (27–30, 30–40, and 19–20, respectively; Jarosewich, 1990) and major element abundances determined by laser ablation are similar.

The existence of composition clusters in plots of trace and minor elements of different volatility, corresponding

Table 2
Major element, Cr, Ni and Co abundances in Paris, Nogoya and in Boriskino determined by ICP-AES and compared with selected literature values for Murchison (F: Friedrich et al. (2002); KW: Kallemeyn and Wasson (1981); MW: Mittlefehldt and Wetherill (1979); WP: Wolf and Palme (2001)). Oxides and loss on ignition (L.O.I.) in wt.% and Cr, Co and Ni in μg/g.

	Paris	Nogoya	Boriskino 1	Boriskino 2	Murchison (literature)
SiO_2	28.72				28.84^{WP}
TiO_2	0.10	0.10	0.10	0.11	0.11^{WP}
Al_2O_3	2.07	1.96	1.95	2.21	2.19^{WP}
Fe_2O_3t	32.05	29.54	30.54	33.02	30.60^{WP}
MnO	0.22	0.22	0.23	0.24	0.22^{WP}
MgO	19.83	18.58	18.43	21.19	20.13^{WP}
CaO	1.61	1.84	1.06	1.51	1.79^{WP}
Na_2O	0.67	0.61	0.57	0.41	0.58^{KW}
K_2O	0.04				0.05^{MW}
P_2O_5	0.28	0.24	0.24	0.25	0.24^{WP}
L.O.I.**	12.88				
Cr	3202	2801	2905	3162	3070WP
Co	651	555	597	649	548^{F}
Ni	14170	12660	13570	14360	12600^{WP}

** Includes 1.93% H, 3.29% C.

to different degrees of volatile depletion, gives us a useful tool for the taxonomy of carbonaceous chondrites (e.g. Kallemeyn et al., 1994). We used such plots to compare both the data by ICP-AES/SFMS (Table 3) and LA-ICP-MS (Table 4) for Paris with other CM, CI and CO chondrites (Kallemeyn and Wasson, 1981; Friedrich et al., 2002; Barrat et al., 2012). Paris falls with the CM chondrites for Zn/Mn vs. Sm/Mn or Al/Mn ratios, and is distinct from CI and CO chondrites.

The REE pattern in Paris is extremely flat and resembles those of most other CM chondrite falls especially Murchison (Fig. 3a). Paris shares the depletion pattern of elements more volatile than Mg (which is smooth with the exception of high Na relative to K) of other CM chondrites, particularly falls (Fig. 3b). Haack et al. (2012) argue that Na is depleted in CMs if, as for the Maribo fall, they are exposed to rain before being collected.

Differences in bulk compositions of fresh and altered matrix are of interest. Abundances of major and volatile elements determined for regions analyzed by LA-ICP-MS (Table 4) are compared with the bulk composition of Paris measured by ICP-AES/SFMS (Tables 2 and 3), and the average bulk composition of CM chondrites measured by radiochemical neutron activation analysis (Wolf et al., 1980) in Fig. 4. As observed by Wolf et al. (1980), CMs reflect a factor of two depletion in the volatile elements relative to CI chondrites, consistent with CMs being a 50:50 mixture of CI-composition matrix and refractory materials (chondrules, etc.), in about the same ratio as observed petrographically (Grossman and Olsen, 1974; McSween, 1979). The bulk composition of Paris determined by LA-ICP-MS (black diamonds) and by ICP-AES/SFMS (gray circles) show the volatile depletion characteristic of CM chondrites (blue squares). The altered matrix analysis is the average of two 50 μm spots (M3/4) analyzed by LA-ICP-MS (red diamonds) and exhibits a volatile-depleted pattern that closely follows the rastered bulk composition with the prominent exception of Li, P, K and Rb. In

Table 3
Trace element abundances (in μg/g) obtained by ICP-SFMS for Paris, Nogoya and Boriskino, and compared with selected literature values for Murchison (F: Friedrich et al. (2002) adjusted to the same standard values as Barrat et al. (2012); N: Nakamura (1974), Tatsumoto et al. (1976).

	Paris	Nogoya	Boriskino 1	Boriskino 2	Murchison	Murchison
					F	N,T
Li	1.60	1.51	1.53	1.61	1.7	
Be	0.0315	0.0317	0.0303	0.0325		
P	1086	1024	997	924		
K	380	397	440	237		
Sc	8.38	7.69	7.93	8.39	8.39	
Ti	628	609	646	629	634	
V	72.1	70.2	73.7	73.7	70	
Cu	128	125	130	123	116	
Zn	180	166	177	168	191	
Ga	7.71	7.45	6.85	7.67	7.34	
Rb	1.72	1.53	1.81	1.07	1.66	
Sr	10.79	10.24	8.01	9.30	10.30	
Y	2.11	1.95	2.05	2.10	2.18	
Zr	4.83	4.51	4.78	5.09	5.1	
Nb	0.384	0.383	0.373	0.410	0.41	
Cs	0.131	0.115	0.132	0.114	0.127	
Ba	3.24	3.00	3.19	2.98	3.23	3.08^{N}
La	0.329	0.311	0.395	0.329	0.314	0.321^{N}
Ce	0.833	0.776	0.974	0.832	0.815	0.848^{N}
Pr	0.126	0.117	0.137	0.126	0.124	
Nd	0.644	0.610	0.675	0.646	0.635	0.641^{N}
Sm	0.211	0.196	0.211	0.212	0.209	0.209^{N}
Eu	0.0797	0.0735	0.0788	0.0801	0.079	0.080^{N}
Gd	0.286	0.273	0.289	0.295	0.282	0.278^{N}
Tb	0.0523	0.0480	0.0525	0.0525	0.052	
Dy	0.351	0.324	0.348	0.355	0.351	0.344^{N}
Ho	0.0769	0.0713	0.0739	0.0763	0.079	
Er	0.225	0.209	0.217	0.225	0.231	0.222^{N}
Tm	0.0355				0.036	
Yb	0.231	0.214	0.229	0.227	0.229	0.226^{N}
Lu	0.0332	0.0305	0.0323	0.0332	0.034	0.036^{N}
Hf	0.144	0.139	0.145	0.154	0.155	
Ta	0.0192	0.0206	0.0192	0.0197		
W	0.073	0.087	0.087	0.134	0.18	
Pb	1.51	1.47	1.75	1.49		1.60^{T}
Th	0.0386	0.0366	0.0404	0.0389	0.039	
U	0.0101	0.00940	0.0103	0.00973	0.0098	0.0110^{T}

Table 4
LA-ICP-MS analyses of section 2010-4 by in-situ rastering of a 0.25 cm^2 square in a comparatively altered region (SP4). Spot analyses by LA-ICP-MS of matrix: M1/2 less altered zone, M3/4 more altered zone.

	Atomic mass		Concentrations	SP4 Average	CI chondrites	M3/4 average	M1/2 average
Li	7	Li7(LR)	µg/g	1.539	1.500	3.117	2.216
Be	9	Be9(LR)	µg/g	0.021	0.025	0.047	0.039
B	11	B11(LR)	µg/g	5.344	0.870	5.761	5.725
Na_2O	23	Na23(LR)	%m/m	0.783	0.674	0.850	1.326
MgO	25	Mg25(LR)	%m/m	21.158	16.400	16.980	17.630
Al_2O_3	27	Al27(LR)	%m/m	2.939	1.640	2.745	3.436
SiO_2	29	Si29(LR)	%m/m	33.787	22.765	31.199	33.851
P_2O_5	31	P31(LR)	%m/m	0.336	0.279	0.465	0.359
S	34	S34(LR)	%m/m	4.796	6.250	5.398	7.004
Cl	35	Cl35(LR)	µg/g	829.924	704.000	700.382	1149.652
K_2O	39	K39(LR)	%m/m	0.092	0.067	0.129	0.151
CaO	44	Ca44(LR)	%m/m	2.289	1.298	3.490	2.266
Sc	45	Sc45(LR)	µg/g	11.218	5.820	7.771	9.041
TiO_2	47	Ti47(LR)	%m/m	0.144	0.073	0.105	0.118
V	51	V51(LR)	µg/g	85.579	56.500	82.895	68.637
Cr	53	Cr53(LR)	µg/g	3812.490	2660.000	3484.190	3369.411
MnO	55	Mn55(LR)	%m/m	0.309	0.257	0.302	0.378
FeO(t)	57	Fe57(LR)	%m/m	33.367	24.495	38.335	33.480
Co	59	Co59(LR)	µg/g	665.524	502.000	740.556	611.397
Ni	60	Ni60(LR)	µg/g	23110.148	11000.000	26083.183	22418.334
Cu	63	Cu63(LR)	µg/g	167.660	126.000	174.263	222.204
Zn	66	Zn66(LR)	µg/g	283.063	312.000	289.094	608.848
Ga	71	Ga71(LR)	µg/g	11.635	10.000	12.040	15.321
Ge	74	Ge74(LR)	µg/g	27.561	32.700	30.424	40.293
As	75	As75(LR)	µg/g	1.706	1.860	1.600	2.217
Se	82	Se82(LR)	µg/g	15.629	18.600	15.868	26.763
Br	79	Br79(LR)	µg/g	18.813	3.570	49.471	67.868
Kr		Kr83(LR)					
Rb	85	Rb85(LR)	µg/g	2.863	2.300	3.513	3.875
Sr	88	Sr88(LR)	µg/g	15.214	7.800	17.611	17.514
Y	89	Y89(LR)	µg/g	2.664	1.560	2.015	2.184
Zr	90	Zr90(LR)	µg/g	6.973	3.940	5.196	5.396
Nb	93	Nb93(LR)	µg/g	0.580	0.246	0.388	0.525
Mo	97	Mo97(LR)	µg/g	1.653	0.928	1.756	1.392
Ru		Ru102(LR)		1.093	0.712	0.988	0.893
Rh	103	Rh103(LR)	µg/g	0.187	0.134	0.157	0.144
Pd	106	Pd106(LR)	µg/g	0.666	0.560	0.598	0.564
Ag	107	Ag107(LR)	µg/g	0.312	0.199	0.240	0.377
Cd	111	Cd111(LR)	µg/g	0.504	0.686	0.545	0.997
In	115	In115(LR)	µg/g	0.070	0.080	0.078	0.127
Sn	120	Sn120(LR)	µg/g	1.057	1.720	1.148	1.632
Sb	121	Sb121(LR)	µg/g	0.148	0.142	0.150	0.246
Te		Te125(LR)		0.762	2.320	0.883	1.648
I		I127(LR)		0.856	0.433	1.410	2.217
Cs	133	Cs133(LR)	µg/g	0.794	0.187	0.706	0.369
Ba	138	Ba138(LR)	µg/g	4.847	2.340	4.689	5.130
La	139	La139(LR)	µg/g	0.452	0.235	0.330	0.410
Ce	140	Ce140(LR)	µg/g	1.174	0.603	0.957	1.053
Pr	141	Pr141(LR)	µg/g	0.170	0.089	0.125	0.146
Nd	145	Nd145(LR)	µg/g	0.885	0.452	0.622	0.748
Sm	147	Sm147(LR)	µg/g	0.295	0.147	0.207	0.251
Eu	153	Eu153(LR)	µg/g	0.117	0.056	0.097	0.127
Gd	158	Gd158(LR)	µg/g	0.381	0.197	0.269	0.303
Tb	159	Tb159(LR)	µg/g	0.067	0.036	0.047	0.054
Dy	164	Dy164(LR)	µg/g	0.476	0.243	0.339	0.365
Ho	165	Ho165(LR)	µg/g	0.101	0.056	0.074	0.085
Er	166	Er166(LR)	µg/g	0.311	0.159	0.224	0.252
Tm	169	Tm169(LR)	µg/g	0.049	0.024	0.032	0.042
Yb	174	Yb174(LR)	µg/g	0.336	0.163	0.213	0.278

Table 4 (*continued*)

	Atomic mass		Concentrations	SP4 Average	CI chondrites	M3/4 average	M1/2 average
Lu	175	Lu175(LR)	μg/g	0.048	0.024	0.034	0.036
Hf	180	Hf180(LR)	μg/g	0.202	0.104	0.138	0.144
Ta	181	Ta181(LR)	μg/g	0.029	0.014	0.021	0.025
W	182	W182(LR)	μg/g	0.183	0.093	0.193	0.151
Re	185	Re185(LR)	μg/g	0.068	0.037	0.046	0.052
Os	192	Os190(LR)	μg/g	0.801	0.486	0.757	0.633
Ir	193	Ir193(LR)	μg/g	0.711	0.481	0.623	0.522
Pt	195	Pt195(LR)	μg/g	1.384	0.990	1.197	1.228
Au	197	Au197(LR)	μg/g	0.385	0.140	0.347	0.384
Hg	202	Hg202(LR)	μg/g	2.939	0.258	2.533	7.034
Tl	205	Tl205(LR)	μg/g	0.162	0.142	0.150	0.219
Pb	208	Pb208(LR)	μg/g	2.994	2.470	2.984	4.902
Bi	209	Bi209(LR)	μg/g	0.131	0.114	0.112	0.192
Th	232	Th232(LR)	μg/g	0.061	0.029	0.035	0.044
U	238	U238(LR)	μg/g	0.017	0.008	0.015	0.017

comparison, the average of two 50 μm spots taken on matrix in unaltered regions (green diamonds) has undepleted abundances like CI chondrite (Zanda et al., 2011a,b).

3.4. Noble gases

All the noble gas characteristics reveal that Paris is clearly linked to the solar gas-rich meteorites. It contains large amounts of light noble gases with ^{4}He and ^{20}Ne concentrations higher than 1×10^{-4} cm^3 g^{-1} and 1×10^{-7} cm^3 g^{-1}, respectively (Table 5). These concentrations are characteristic of gas-rich meteorites (Eugster et al., 2007) and are best explained by the occurrence of a solar wind component. This is confirmed by the ^{4}He/^{20}Ne ratio that falls within the range determined for the Solar gas-rich meteorites (Eugster et al., 2007). In addition, the low ^{3}He/^{4}He of 3.4–4.2 $\times 10^{-4}$ (Table 5) are near the range of solar values ($4.64 \pm 0.09 \times 10^{-4}$, Heber et al., 2009) but differ from other He components trapped in gas-poor meteorites. Likewise, the ^{20}Ne/^{22}Ne ratios of 9.61–11.42 indicate the presence of solar noble gases (13.78 ± 0.03; Heber et al., 2009).

The ^{20}Ne/^{36}Ar ratio and the argon and xenon isotopic compositions (Fig. 5, Tables 5 and 6) point out that the so-called Q component (a ubiquitous noble gas component trapped in chondrites; Busemann et al., 2000) is also present in Paris. This component, trapped in the insoluble organic matter of primitive meteorites (Marrocchi et al., 2005), dominates the heavy noble gas signature of Paris in good agreement with the noble gas characteristics of other CMs (Busemann et al., 2000).

The cosmic-ray exposure age (hereafter CRE age) represents the time of exposure to the galactic cosmic rays of a meter-sized meteoroid until its capture by the Earth. This duration can be calculated from the excess of ^{3}He$_{cos}$, ^{21}Ne$_{cos}$ and ^{38}Ar$_{cos}$ relative to solar isotopic composition. Cosmogenic production rates of ^{3}He$_{cos}$, ^{21}Ne$_{cos}$ and ^{38}Ar$_{cos}$ were computed from the chemical composition of Paris determined in this study (Table 2) and following the procedure of Eugster and Michel (1995). We also determined the concentration of ^{3}He$_{cos}$, ^{21}Ne$_{cos}$ and ^{38}Ar$_{cos}$ from the heating extraction data using the protocol proposed by Eugster et al. (2007). Due to the high abundance of ^{4}He of Paris ($>2 \times 10^{-5}$ cm^3 g^{-1}; Table 5), we took into account the contribution of radiogenic ^{4}He from U and Th decay on the calculated abundance of ^{3}He$_{cos}$ (Eugster et al., 2007). As the amounts of U and Th of Paris have not been determined, we used the average concentration in CM chondrites to determine the abundance of radiogenic ^{4}He (Wasson and Kallemeyn, 1988). The ^{3}He$_{c}$ ages are 2.81 ± 0.41 and 2.75 ± 0.18 Ma for samples A and B, respectively (Table 7), in good agreement with the ^{21}Ne$_{c}$ ages of 3.65 ± 0.10 and 3.55 ± 0.08 Ma. The ^{38}Ar$_{c}$ ages were not determined because the argon content of Paris is dominated by the Q component, precluding a good estimation of the abundance of cosmogenic ^{38}Ar. The CRE ages determined for Paris fall within the range of those reported for other CM carbonaceous chondrites that are characterized by short CRE ages (Eugster et al., 2006). The reasons why CMs have such short exposure ages are not quite clear but might be linked to their fragile natures that reduce their ability to survive under space conditions (Scherer and Schultz, 2000). In any case, the noble gas signatures reported in this study anchor Paris into the gas-rich meteorite clan and present characteristics close to the CM carbonaceous chondrites.

4. PETROGRAPHY, MATRIX AND ALTERATION

4.1. Petrographic overview

Paris contains more abundant, well preserved metal in Type I chondrules and in matrix than other CMs. Type Im (metal-bearing) granular/porphyritic chondrules (McSween, 1977) are especially prominent. We show a BSE image of Paris 2010-04 (Fig. 6), with contrast such that forsterite is dark grey, ferroan olivine and PCP are light grey and metal is white. The chondrite is less altered at the bottom left and more altered at the top right: the contrast in metal abundance between the fresher and more altered domains is striking. There is approximately 3% metal

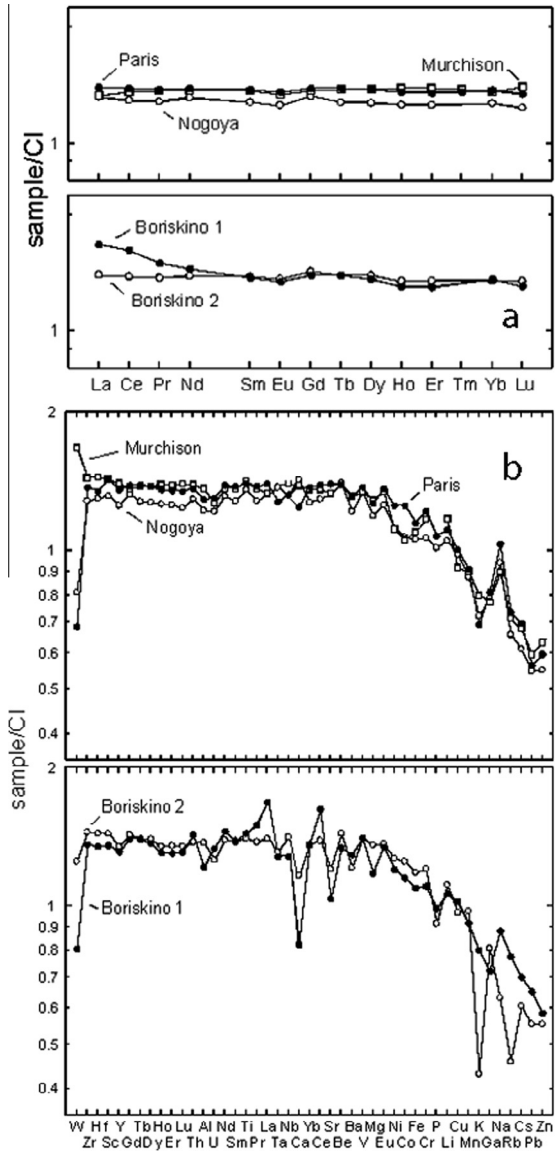

Fig. 3. Analyses of (a) REE and (b) other elements, in Paris and other CM chondrites by SFMS. Paris shows the volatile element depletion typical of CM chondrites, and is almost identical to Murchison.

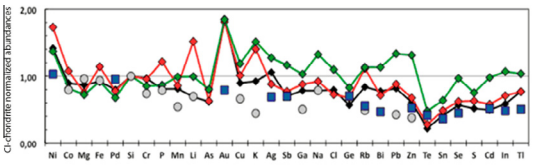

Blue squares: average CM2 bulk composition (Wolf et al., 1980).
Grey dots: bulk chemistry data (UBO); aliquot from a 13g powder.
Diamonds and lines: LA-ICP-MS data (NHMFL) measured *in situ* on 2010-04.
Black: bulk composition of the altered region obtained by rastering 0.25 cm^2 .
Red: average of 2 spots in the matrix of altered regions (M3-M4);
Green: average of 2 spots in the matrix of least altered regions (M1-M2).

Fig. 4. CI- and Si-normalized abundances of major and volatile elements determined by LA-ICP-MS from petrographically chosen contexts in different Paris regions (bulk, more altered and less altered matrix) as a function of condensation temperature. (For interpretation of the references to color in this figure legend, the reader is referred to the web version of this article.)

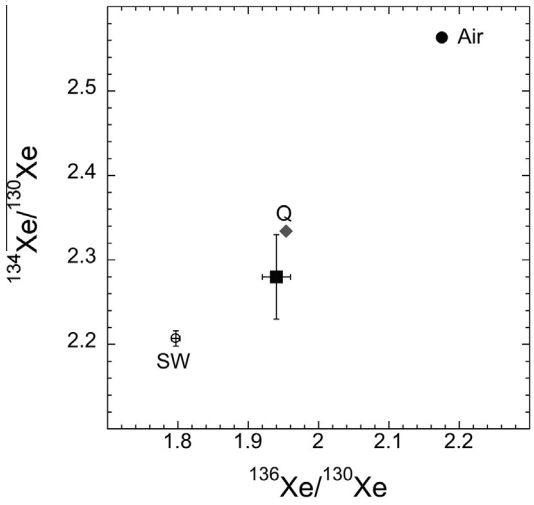

Fig. 5. Bulk $^{136}Xe/^{130}Xe$ and $^{134}Xe/^{130}Xe$ ratios of Paris (filled square) determined with a CO_2 laser. The results show that the typical Q component dominates the heavy noble gas signature of Paris in accordance with the noble gas characteristics of other CMs (Busemann et al., 2000). Air composition data are from Ozima and Podosek (2002). Q-Xe composition data were obtained by closed-system sample etching (CSSE) on 8 different meteorites (Busemann et al., 2000). Solar wind data (SW) are from Wieler and Baur (1994).

in the freshest areas, mainly within Type I chondrules, but only traces of metal in the most altered areas. The least altered CM chondrite studied by Rubin et al. (2007) is QUE 97990, which contains ~1% metal. Type II chondrules (<2%), refractory inclusions (<1%), and chondrule debris are also present in Paris. Chondrule silicate minerals are fresh and unserpentinized. Chondrule glass is preserved in inclusions in olivine, especially in Type II chondrules, but is replaced in mesostasis by aluminous serpentine (Table 8). The preservation of chondrules in Paris leaves little doubt that the loose sugary aggregates of olivine and olivine crystal clasts in highly altered CM chondrites are derived from chondrules. Although there are several lithic clasts in Paris, we do not recognize clastic matrix, suggesting it is mainly "primary rock" (Metzler et al., 1992).

The mineralogical composition of altered matrix varies widely, as seen in BSE as regions of different average grey tones. The widespread CM material "PCP" has been shown by a large body of work (Tomeoka and Buseck, 1985; Browning et al., 1996; Rubin et al., 2007; Palmer, 2009) to be intergrowths of cronstedtite and tochilinite. In Paris, however, intergrowths are very fine grained, may have compositions poorer in both Si and S than expected, and contain other phases including nano-magnetite. Their composition and abundance are variable. We therefore prefer to retain the term PCP. There are darker domains in BSE images with chondrules containing fresh metal in gradational contact with zones with altered metal and prominent bright grey PCP grains, e.g. in 2010-4 (Fig. 7a, a close-up of the center of Fig. 6). There are also sharp

Table 5
Helium, neon and argon concentration ($cm^3\ g^{-1}$) and isotopic ratios for Solar gas-rich meteorites, Q-gases and two fragments of Paris. The listed uncertainties on abundances and isotopic ratios (1σ) include blank, standard and sample uncertainties

Sample	mass (mg)	laser steps	^3He ($10^{-8}\ cm^3\ g^{-1}$)	$^3He/^4He$ ($\times10^{-4}$)	^{21}Ne ($10^{-9}\ cm^3\ g^{-1}$)	$^{20}Ne/^{22}Ne$	$^{21}Ne/^{22}Ne$	^{38}Ar ($10^{-7}\ cm^3\ g^{-1}$)	$^{38}Ar/^{36}Ar$	$^{40}Ar/^{36}Ar$	$^4He/^{20}Ne$	$^{20}Ne/^{36}Ar$
Paris-A	0.106	2	23.68 (1.81)	3.40 (0.31)	15.93 (0.51)	11.42 (0.24)	0.079 (0.004)	3.53 (0.03)	0.188 (0.002)	9.2 (0.2)	278.36 (0.02)	1.42 (0.01)
Paris-B	0.295	4	13.73 (0.80)	4.21 (0.30)	12.88 (0.33)	9.61 (0.18)	0.110 (0.005)	3.04 (0.02)	0.189 (0.001)	9.7 (0.2)	267.73 (0.02)	0.82 (0.01)
Solar gas-rich meteorite[a]				3.02 (0.04)		12.24 (0.30)	0.032 (0.016)		0.179 (0.005)	120–600		47 (3)
Q[b]				1.23 (0.02)		10.67 (0.02)	0.029 (0.001)		0.187 (0.003)	112 (10)		0.044 (0.006)

[a] Gas-rich meteorites composition determined by Eugster et al. (2007)
[b] Q-gas composition data obtained by closed-system sample etching (CSSE) on 8 different meteorites (Busemann et al., 2000)

Table 6
Xe concentration ($cm^3\ g^{-1}$) and isotopic ratio for Air, Solar wind, Q-gases and one fragment of Paris. Isotopic ratios × 100. The listed uncertainties on abundances and isotopic ratios (1σ) include blank, standard and sample uncertainties.

Sample	laser steps	mass (mg)	^{130}Xe ($10^{-10}\ cm^3{\cdot}g^{-1}$)	$^{124}Xe/^{130}Xe$	$^{126}Xe/^{130}Xe$	$^{128}Xe/^{130}Xe$	$^{129}Xe/^{130}Xe$	$^{131}Xe/^{130}Xe$	$^{132}Xe/^{130}Xe$	$^{134}Xe/^{130}Xe$	$^{136}Xe/^{130}Xe$
Paris-B	4	0.295	4.57 (0.03)	2.911 (0.14)	4.357 (0.17)	50.20 (0.70)	624.0 (6.8)	487.0 (5.2)	603.0 (6.0)	228.1 (2.9)	193.8 (2.3)
Air[*]				2.337 (0.008)	2.180 (0.011)	47.15 (0.07)	649.6 (0.6)	521.3 (0.6)	660.7 (0.5)	256.3 (0.4)	217.6 (0.2)
Q[**]				2.810 (0.004)	2.505 (0.018)	50.79 (0.02)	645.9 (0.2)	506.4 (0.3)	617.5 (0.2)	233.4 (0.2)	195.4 (0.2)
SW[***]				2.948 (0.017)	2.549 (0.082)	51.02 (0.54)	627.3 (0.5)	498.0 (0.2)	602.0 (0.3)	220.7 (0.9)	179.7 (0.6)

[*] Air composition data are from Ozima and Podosek (2002).
[**] Q-gas composition data obtained by closed-system sample etching (CSSE) on 8 different meteorites (Busemann et al., 2000).
[***] Lunar soil 75101 by the CSSE method (Wieler and Baur, 1994).

Table 7
Production rates and CRE ages determined for Paris from the abundances of cosmogenic light noble gases.

	Production rate (10^{-8} cm^3 STP/g, Ma			CRE ages		
	P_3	P_{21}	P_{38}	T_3	T_{21}	T_{38}
Paris-A	1.584	0.294	0.0539	2.81 (0.41)	3.65 (0.10)	–
Paris-B	1.584	0.294	0.0539	2.75 (0.18)	3.55 (0.08)	–

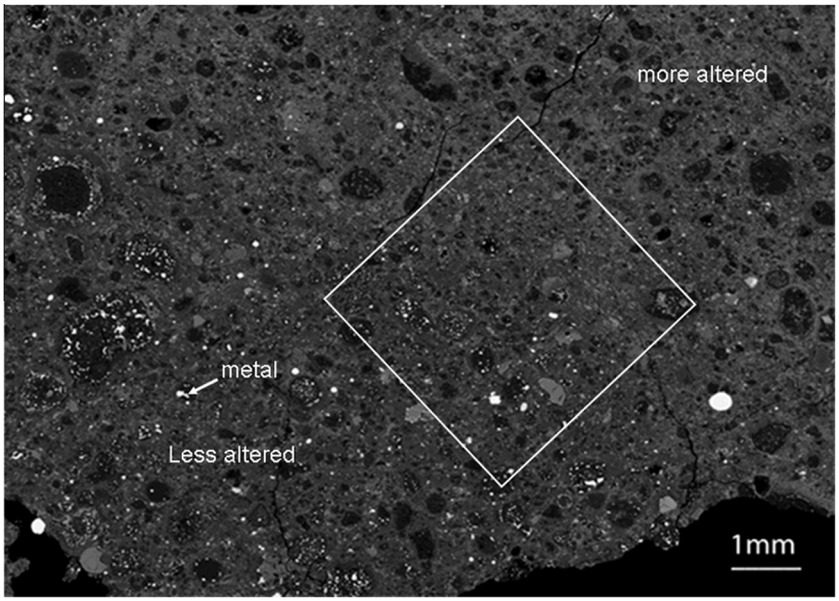

Fig. 6. BSE image of Paris section 2010-04 with metal (white), ferroan olivine (bright grey), matrix phases (light-dark grey) and magnesian olivine plus pyroxene (very dark gray). Broad gradational contact from top left to bottom right. Metal is abundant in Type I chondrules in the fresh domain near bottom left and but is replaced in the moderately altered domain near top right. The white rectangle shows the location of Fig. 7a.

Table 8
Averages (wt.%) and *standard deviations* for EMP analyses of alteration material.

	SiO_2	Al2O3	TiO2	"Cr2O3"	"FeO"	MnO	MgO	CaO	Na2O	K2O	"P2O5"	S	Ni	Total
Serpentine *matrix*	27.17	2.86	0.07	0.41	33.72	0.27	14.34	0.49	0.52	0.07	0.16	2.96	1.92	84.95
Serpentine *chondrule*	25.49	7.46	0.48	0.07	33.57	0.33	10.01	0.93	1.00	0.09	0.77	0.50	0.07	80.77
Cronstedtite	19.34	2.85	0.04	0.11	48.85	0.19	6.94	0.20	0.42	0.04	0.10	2.57	0.94	82.60
PCP I	10.81	3.21	0.03	0.18	53.18	0.14	5.54	0.14	0.50	0.05	0.08	9.03	1.60	84.50
PCP II, $n = 5$	5.33	5.05	0.02	0.29	53.27	0.14	4.32	2.14	0.82	0.04	1.19	5.43	1.11	79.17
PCP II, $n = 4$	2.90	1.93	0.01	0.03	67.25	0.12	3.59	0.06	0.40	0.02	0.03	3.95	0.57	80.87
T-I tochilinite	6.53	0.25	0.04	3.12	53.23	0.31	0.84	0.65	0.28	0.04	3.81	7.61	9.20	85.91
T-II tochilinite, $n = 2$	3.22	2.17	0.03	0.07	63.92	0.07	3.50	0.01	0.14	0.00	0.01	18.38	1.71	93.23
T-II tochilinite, $n = 7$	2.21	1.78	0.01	0.06	62.68	0.13	3.86	0.09	0.31	0.02	0.01	13.51	0.56	85.23
T-II tochilinite, $n = 2$	1.08	1.95	0.01	0.03	69.53	0.16	2.93	0.07	0.38	0.01	0.00	4.53	0.43	81.10
Magnetite	0.08	0.02	0.01	0.05	88.33	0.03	0.01	0.05	0.04	0.00	0.03	0.01	0.04	88.71
Serp matrix, n = 20	2.82	0.69	0.04	0.23	5.59	0.08	2.56	0.34	0.18	0.04	0.05	0.97	0.65	2.43
Serp chondrule, n = 6	*4.11*	*2.04*	*0.27*	*0.22*	*9.65*	*0.14*	*2.47*	*1.46*	*0.26*	*0.06*	*0.74*	*0.33*	*0.04*	*5.96*
Cron, n = 9	2.28	1.35	0.02	0.08	6.71	0.04	1.89	0.15	0.26	0.04	0.16	1.75	0.82	1.51
PCP I, n = 29	*5.13*	*1.96*	*0.02*	*0.58*	*5.93*	*0.07*	*1.74*	*0.15*	*0.28*	*0.03*	*0.19*	*4.60*	*2.05*	*4.09*
PCP II, n = 5	*2.10*	*2.56*	*0.02*	*0.53*	*3.60*	*0.07*	*1.49*	*4.60*	*0.21*	*0.02*	*2.56*	*1.74*	*1.20*	*6.20*
PCP, II, n = 4	*2.16*	*0.67*	*0.01*	*0.02*	*2.86*	*0.05*	*0.82*	*0.03*	*0.09*	*0.02*	*0.03*	*0.90*	*0.26*	*1.29*
T-I, n = 6	*0.77*	*0.15*	*0.08*	*0.24*	*1.85*	*0.06*	*0.27*	*0.09*	*0.43*	*0.01*	*0.34*	*0.92*	*1.93*	*1.81*
T II, n = 2	*0.76*	*0.77*	*0.02*	*0.01*	*1.58*	*0.02*	*1.87*	*0.02*	*0.19*	*0.00*	*0.01*	*3.24*	*1.82*	*4.94*
T-II, n = 7	*1.05*	*0.41*	*0.01*	*0.05*	*2.87*	*0.06*	*1.25*	*0.06*	*0.06*	*0.01*	*0.01*	*1.68*	*0.40*	*3.46*
T-II, n = 2	*0.23*	*0.76*	*0.02*	*0.02*	*1.70*	*0.01*	*0.48*	*0.02*	*0.05*	*0.02*	*0.00*	*0.99*	*0.13*	*1.99*
Mag, n = 4	*0.04*	*0.02*	*0.01*	*0.03*	*0.30*	*0.04*	*0.01*	*0.04*	*0.04*	*0.00*	*0.03*	*0.00*	*0.04*	*0.33*

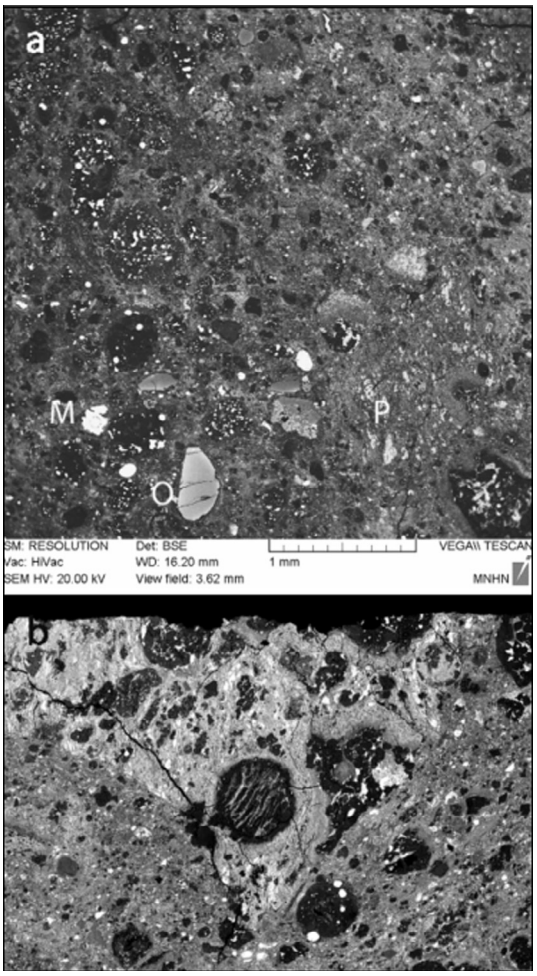

Fig. 7. (a) Gradational contact, vertical in the center of the figure, in Paris section 2010-4 between fresh CM material on left (part of region in Fig. 6), with Type I chondrules containing small fresh metal globules, and altered CM material on right, containing abundant PCP (bright grey) and chondrules with altered metal. M, O and P are adjacent to metal, olivine and PCP, respectively. (b) Sharp contact in Paris between moderately altered CM material and bright PCP-rich clast at top in 2010-1 (image width 2.6 mm).

contacts, e.g. in 2010-1 (Fig. 7b), between moderately altered matrix and angular bodies of BSE-bright material rich in PCP.

4.2. Matrix mineralogy

4.2.1. Matrix petrography

The matrix in Paris appears in BSE to consist mainly of fine-grained mixtures of phyllosilicates (cronstedtite–chrysotile–greenalite solid solutions), tochilinite-like material and PCP (mixtures or intergrowths containing the above phases). The size and abundance of PCP (bright grey in Fig. 7) varies with extent of alteration. Pyrrhotite, pentlandite and Fe–Ni–P–S sulfides are observed in phyllosilicate-rich matrix. There are a few large irregularly shaped isolated polycrystalline Fe–Ni sulfide grains, up to 80 μm in maximum dimensions (3 grains observed in thin sections 2010-7 and -8). These grains consist of pyrrhotite rimmed with small pentlandite flames or granules in a more or less continuous peripheral corona (Fig. 8a and b). Semi-quantitative EDS analyses indicate metal/sulfur ratio (at.) close to 0.9 in hexagonal pyrrhotite (Hpo) and Fe/Ni at. = 1.2–1.4 in Fe-rich pentlandite (Pn, richer in Ni than matrix pentlandite). Some enclose spherical forsterite droplets which show Fe-enriched rims in contact with the pyrrhotite. Pt–Ir–(Os) alloys (2–3 μm) have been detected in two grains (former refractory metal nuggets (RMN) completely re-equilibrated with pyrrhotite for the most chalcophile PGEs Ru, Rh and Pd). Type II chondrules contain an Fe sulfide with ~1% Ni and the same stoichiometry as Canyon Diablo troilite, and a similar sulfide is found in matrix; its survival suggests limited alteration. Metal in matrix is derived from Type I chondrules and may contain inclusions, e.g. of silica (Fig. 8d). It shows thin rims of tochilinite in the freshest zones (Fig. 8c), but is extensively replaced in the more altered regions.

TEM images of the matrix reveal a complex fine-grained assemblage dominated by an amorphous phase, as in Y-791198 (Chizmadia and Brearley, 2008), and phyllosilicates (Fig. 9). Anhydrous silicates, sulfides and carbonaceous matter are also present. The most abundant phase displays a mottled contrast and a sponge-like structure with numerous nano-sized voids (Fig. 9a). Electron diffraction patterns show a diffuse ring indicative of amorphous or poorly crystalline material. Locally a fibrous morphology is clearly distinguishable from the matrix amorphous material, with a gradation in size suggesting a continuum from the sponge-like structure to a coarse-grained fibrous morphology. Only the coarse-grained areas (Fig. 9b) display a crystalline signal in electron diffraction, compatible with a serpentine structure.

The FIB samples also contain relatively large and elongated grains suggesting plate morphology. Their widths are typically a hundred to several hundreds of nanometers and they can reach several micrometers in length. The electron diffraction patterns (Fig. 10a) and compositions indicate the solid solution cronstedtite–thüringite–amesite, where thuringite is $(Fe^{2+}, Fe^{3+}, Mg, Al)_6(Si, Al)_4O_{10}(O, OH)_8$ and amesite is $(Mg, Al)_3(Si, Al)_2O_5(OH)_4$.

They are iron-rich and are termed cronstedtite in the following. Discrete cronstedtite crystals are rarer and tiny (~100 nm) in chondrule rims but larger and polycrystalline in adjacent matrix, as in Y-791198 (Chizmadia and Brearley, 2008). Fig 10a shows large laths of cronstedtite with fine interstratified tochilinite (blue arrows) and associated fibrous regions (red arrows). Cronstedtite and fibrous material are coarser in the matrix of more altered zones. Tochilinite seen in TEM is mainly a sulfur-rich fibrous phase, varying in morphology and crystallinity in different regions. The fibrous regions replacing metal in a chondrule are locally surrounded by an iron oxide phase, probably magnetite, with many crystal defects (Fig. 10b).

Anhydrous silicates seen in TEM images consist of forsterite and enstatite. Most of them have a rounded morphology (Fig. 11a) and are micron to sub-micron in size. Some of the enstatite grains are elongated along the [1 0 0] direction. Enstatite contains numerous planar defects

(ortho-clino inversion) on (100). In rare cases part of an enstatite grain is replaced by fibrous Fe-bearing serpentine. Other accessory minerals are Ca-phosphate, Cr–Al spinels and hollow carbon globules (Fig. 11b). Carbonates were not detected in these TEM-FIB sections but the more altered matrix domains contain 1–3% calcite, ~50 μm in diameter, particularly associated with altered CAI. Dolomite and more complex carbonates were not recognized.

Magnetite spherules, partly clustered into framboids (Fig. 12a), are present in very restricted domains, in which metal in contact with matrix is quite altered. Although magnetite may be observed in significant amount in some FIB sections (Fig. 10b), BSE imaging suggests magnetite is a trace mineral. However, a precise estimate of a maximum magnetite content of 6.4 wt.% was made from magnetic measurements in §4.2. The magnetite in Fig. 12a occurs in a clast 1.8 mm across sharply distinguished from surrounding matrix much more enriched in PCP-related material (Fig. 12b). The magnetite is concentrated in clast matrix between the fine-grained rims on Type I chondrules.

4.2.2. Matrix mineral compositions

The matrix was analyzed using EPMA, using Si, Fe, Mg and S concentrations to identify the main minerals under the beam, and ATEM (Tables 8 and 10). Note that the characterization of phases is not parallel at the different scales of observation, as discussed in detail below. As the amorphous phase (Fig. 8) does not have a distinctive stoichiometry, we could not identify it by EMPA. Thus some, perhaps most, of our 'serpentine' is probably a mixture of the amorphous phase with cronstedtite and/or other phases. The EMP data for serpentine and cronstedtite, plus intergrowths (PCP), tochilinite-like material and (rare) magnetite in matrix in Paris section 2010-04 and 2008-LM are summarized in Table 8 and shown in Fig. 13. We found only slightly different compositions of phases in regions of different degrees of alteration (Section 6.1). The phyllosilicate endmember compositions are also plotted in the Mg–Si–Fe quadrilateral (Fig. 13a) and it is seen that phyllosilicates run from about $Chrysotile_{60}$–$Greenalite_{40}$ to about $Chrysotile_{20}$–$Cronstedtite_{80}$.

TEM work performed on FIB sections of fine-grained rims on chondrules and chondrite matrix in moderately altered regions of section SPSR-1 permitted precise identification of phases (Table 9 and Fig. 14a and b). Compositions of the abundant amorphous phase and the finest fibers are comparable to the serpentine in Fig. 13, but more Si-rich. They cross the chrysotile–greenalite join and extend to the

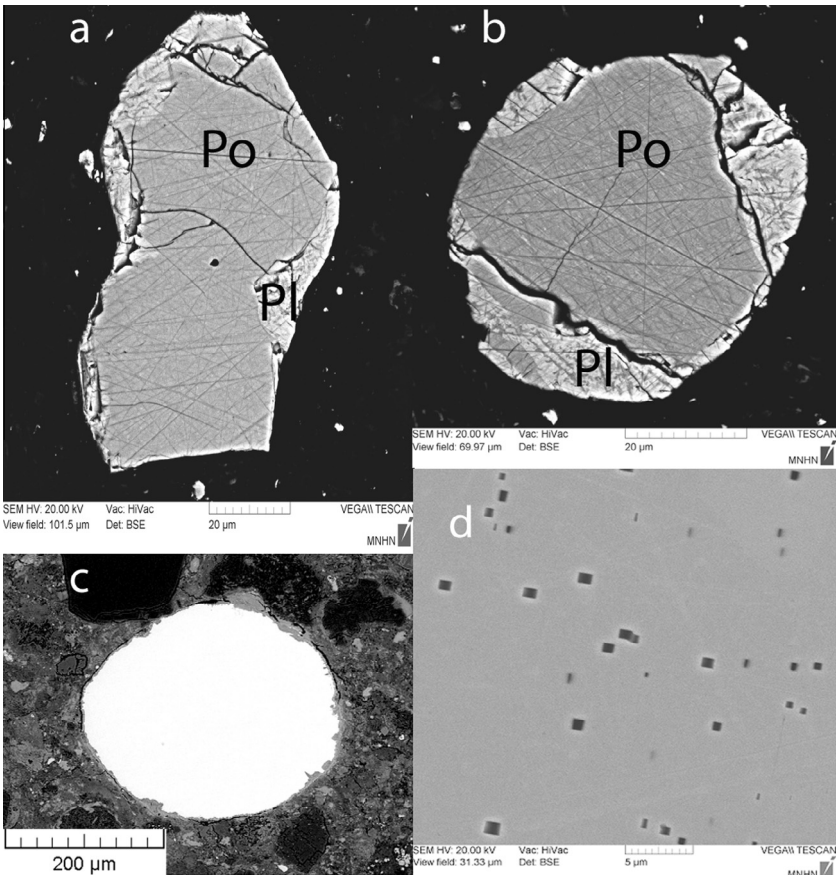

Fig. 8. (a and b) Grains of pyrrhotite rimmed with small pentlandite granules in a more or less continuous peripheral corona in Paris matrix. (c) Metal grain (300 μm) in a more altered part of 2010-04, outside the right edge of Fig 7a, with a tochilinite rim ~2–10 μm thick (d) Euhedral precipitates of silica exsolved in kamacite formed in Type I chondrules indicate mild reheating or slow cooling.

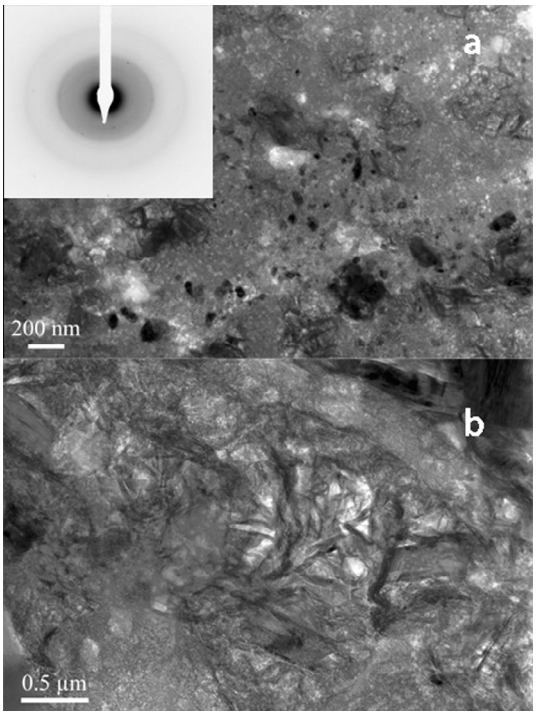

Fig. 9. Bright field TEM images. (a) Amorphous silicate with a mottled contrast and a sponge-like structure containing numerous nano-sized voids. The inset shows its electron diffraction pattern. Wispy fibrous phyllosilicate and dark sulfide inclusions are also present. (b) Well developed fibrous serpentine region.

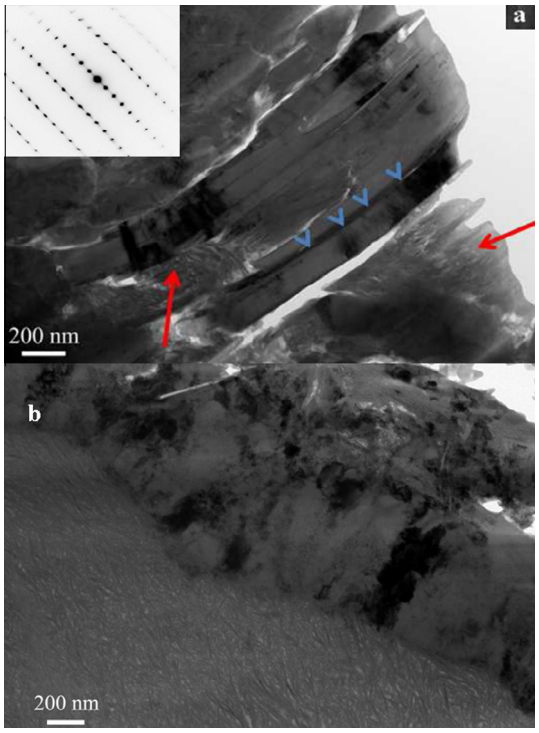

Fig. 10. Bright field TEM images in altered region. (a) Large laths of cronstedtite with interstratified tochilinite (blue arrows) and fibrous serpentine (red arrows). The inset shows an electron diffraction pattern of the cronstedtite. (b) PCP on chondrule rim. Fibrous tochilinite at the bottom, presumably in replacement of an iron-sulfide grain. The S-rich fibrous region is surrounded by a thick iron-oxide layer (middle/top) at the interface with a silicate. Small grains at top right are colloidal silica polishing material. (For interpretation of the references to color in this figure legend, the reader is referred to the web version of this article.)

En–Fs join (Fig. 14a), suggesting a variable amount of Si and a low fraction of crystalline phyllosilicate mixed in with the amorphous material. They are similar to the average compositions of amorphous material in other primitive material (GEMS in interplanetary dust particles, Acfer 094, ALH 77307, MET 00246, QUE 99177 and Yamato 791198: Brearley, 1993; Chizmadia and Brearley, 2008; Abreu and Brearley, 2010; Keller and Messenger, 2012).

Coarser-grained fibers are richer in Fe than the sponge-like areas and the ratio Si/(Mg + Fe) decreases with increasing fiber width displacing the compositions towards the chrysotile–cronstedtite join (Fig 14a). They are similar in composition to the most Si-rich PCP-I of Fig. 13. The gradation in size and composition suggests a close relationship between the amorphous (sponge-like) areas and the coarse grained fibrous areas. Ni-rich and Ni-poor sulfides, pyrrhotite and pentlandite, are widespread in the amorphous material, with an average size of 50 nm (Fig. 8a). Sulfide grains are not present in the fibrous areas but S is still detectable in abundance, suggesting that it is located in the interstratified layers of phyllosilicates or expressed as nanometer-scale tochilinite grains. Thus the coarse fibrous material might be considered a nano-PCP. Platy/elongated crystals (cronstedtite) are more Fe-rich and Al-rich (Table 9) than the amorphous material. They generally have less S than the cronstedtite of Fig. 13, but some regions are interstratified with thin layers of tochilinite.

We analyzed several varieties of tochilinite-like material by EMP (Table 8), including some with compositions close to that of the most Si-poor tochilinite of Tomeoka and Buseck (1985) and Palmer (2009). Many grains are richer in Si and poorer in S than this, in part because of intergrowth with cronstedtite. However there is a variety (tochilinite I in Table 8), which is S-poor but Cr–P–Ni-rich and Mg-poor, with affinities to the metal-derived Type I PCP of Tomeoka and Buseck (1985). This composition may indicate the presence of schreibersite or P-rich sulfides (Palmer, 2009; Nazarov et al., 2009). Tochilinite II (poor in Cr–P–Ni) varies from close to the Fe tochilinite endmember to poor in both Si and S (Fig. 13b). Its composition approaches that of altered metal and it may contain an Fe-rich phase. ATEM analyses of tochilinite are shown in Table 9 and Fig. 14. Where it is very crystalline, it contains no Si (Fig. 14a). Where it is finely fibrous, there is Si and also abundant Ni. The high proportion of Si likely indicates a mixture with phyllosilicates.

Most PCP intergrowth compositions fall between cronstedtite and tochilinite (Fig. 13a and b). We distinguish them in Table 8 as PCP I and they fit the PCP SiO_2 criterion of Rubin et al. (2007). Blanchard et al. (2011) reported similar compositions of PCP in Paris sections 2010-5 and -7. However we also observe PCP-like material, PCP II, which is depleted in both S and Si, plotting on the Fe-rich side of the tochilinite–cronstedtite tie line. This material

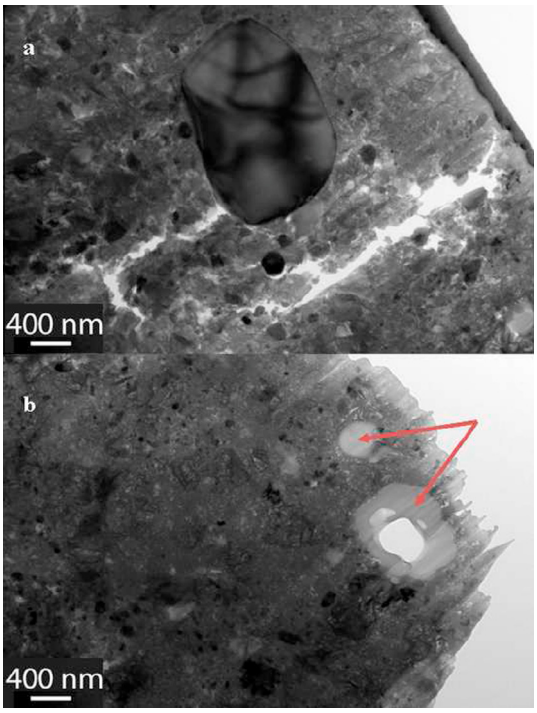

Fig. 11. Bright field TEM images. (a) Large grain of forsterite in fine grained matrix. (b) Hollow carbon nanoglobules (arrows) in matrix.

approaches altered metal in composition (Fig. 13b) and is mixtures of tochilinite, phyllosilicate and some Fe-rich phase related to alteration of metal, probably magnetite, as seen in association with tochilinite fibers in Fig. 10b.

4.3. Magnetic properties and mineralogy

Elmaleh et al. (2011, 2012) compared the low-temperate (2–300 K) magnetic properties of single crystals of cronstedtite, and of CM2 chondrites including Paris. The temperature of the magnetic susceptibility peak (Tp, 7 K) of cronstedtite falls with increasing Mg and increases in interacting fine grained particles. Elmaleh et al. (2012) observe a decrease of Tp among the CM chondrites with increased alteration based on the mineralogical alteration index (Browning et al., 1996) and the FeO/SiO_2 content of PCPs (Rubin et al., 2007). Metal-rich and metal-poor areas in the Paris chondrite show contrasting low-T magnetic signatures, with a shift from high Tp in the less altered material to a lower one like Murray's. The evolution of the low-T magnetic signature is interpreted as due to changes in cronstedtite's chemical composition (Elmaleh et al., 2012).

We measured the magnetic susceptibility of Paris on two large samples, both with masses of 17.1 g, as $\log\chi = 4.310$ and 4.50 (χ^2 in $10^{-10}\,m^3\,kg^{-1}$). The mean $\log\chi = 4.45$ is in the very upper range for CM chondrites, that have mean susceptibility $\log\chi = 3.100 \pm 0.43$, computed from 52 CM chondrites (Rochette et al., 2008). As shown by measurements taken on 12 samples with mass ranging from 23 mg to 17.1 g, magnetic susceptibility is homogeneous down to the scale of ~2 g. Below 2 g, there is an increasing scatter between measurements: the four measurements on masses

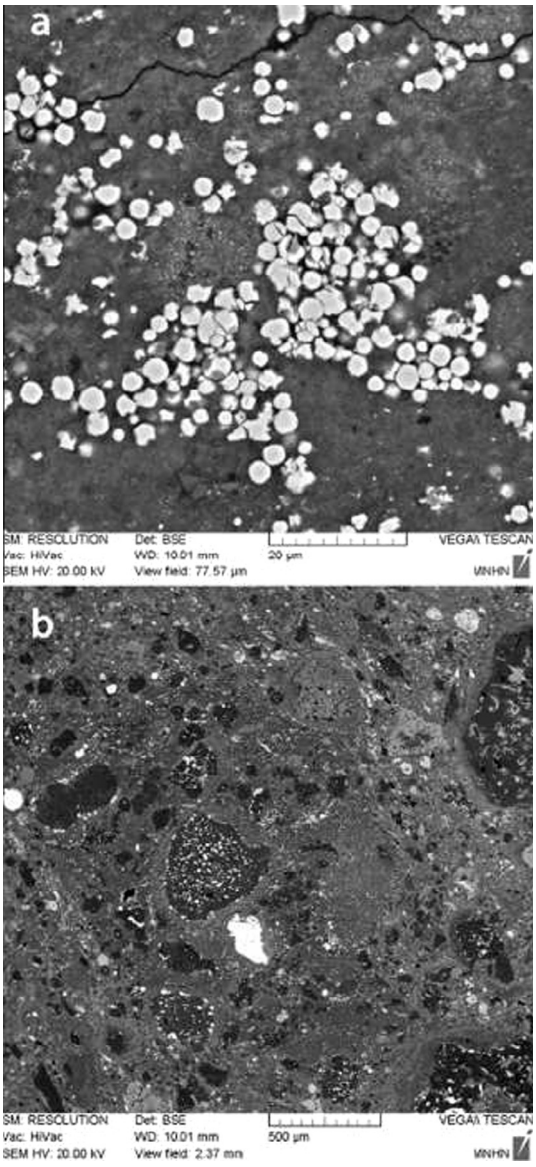

Fig. 12. (a) Detail of magnetite framboids (b) Fragment 1.8 mm across containing magnetite spherules, and with a metal-rich chondrule near its center, is in sharp contact with normal altered matrix with PCP at top and right.

between 1 and 2 g give an average $\log\chi = 4.33 \pm 0.23$, and the five measurements on masses below 1 g give an average $\log\chi = 4.47 \pm 0.40$.

Monitoring of magnetic susceptibility at low temperature performed on six samples with mass in the 20–100 mg range shows the existence of a weak Verwey transition in all samples but one, indicating the presence of stoichiometric magnetite with variable abundance at this scale (Fig. 15). This is confirmed by cooling of room temperature saturation isothermal remanent magnetization (SIRM), as well as heating of low temperature SIRM that also shows the Verwey transition (Fig. 16). It is noteworthy that the only sample that does not display a Verwey transition is the sample that was specifically sampled in the less aqueously altered lithology of the meteorite, whereas the sample that

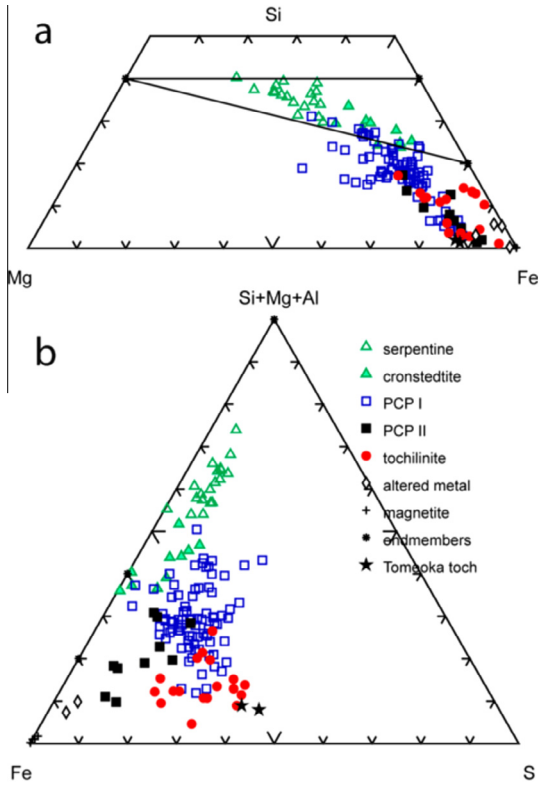

Fig. 13. EMPA data (at.%) of 300 nm squares of Paris matrix alteration materials, named for the dominant mineral present. The Fe concentration is total Fe in the spot analyzed (silicate ± sulfide). Asterisks are end-member chrysotile, greenalite and cronstedtite compositions; stars are the most Si-poor Type I and II tochilinite of Tomeoka and Buseck (1985).

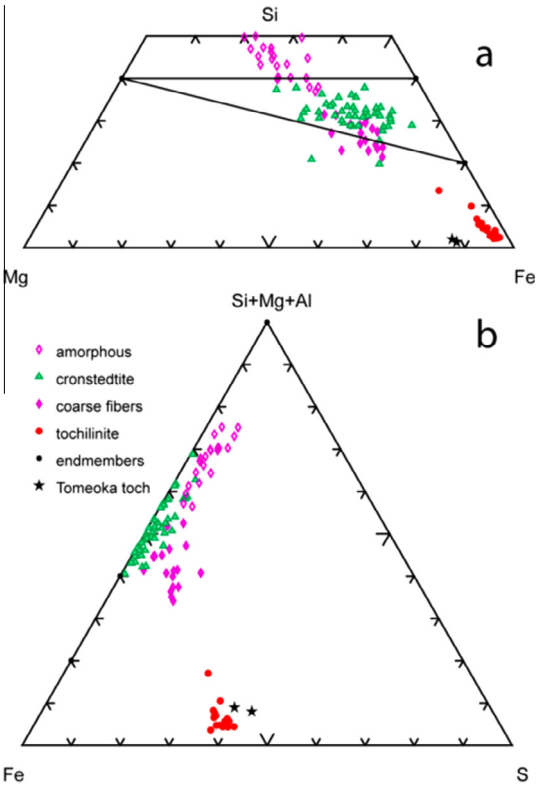

Fig. 14. ATEM data (at.%) for Paris matrix alteration materials, corrected for the presence of sulfide inclusions. Amorphous refers to mottled and porous material, and finely fibrous material. End-member chrysotile, greenalite and cronstedtite compositions are also shown, plus the most Si-poor Type I and II tochilinite of Tomeoka and Buseck (1985).

shows the strongest Verwey transition is the one that was specifically sampled in the more aqueously altered lithology.

High temperature measurements of magnetic susceptibility under argon atmosphere (Fig. 17a) show Curie temperatures at 581 °C, corresponding to magnetite. The residual magnetic susceptibility above 585 °C is due to the presence of metallic FeNi. However, it is not possible to determine the Ni content of this phase because it is being destroyed during the heating experiment, as indicated by the irreversible curve upon cooling, with formation of new magnetite (Fig. 17a). The S ratio of 0.83 ± 0.05 ($n = 4$) indicates that in addition to magnetite and FeNi metal, Paris contains a mineral with high coercivity, suggesting the presence of sulfides.

Table 9
Averages (at.%) and *standard deviations* for TEM analyses of matrix phases. Data are normalized to a 100% anhydrous basis.

	Si	Al	Fe	Mg	S	Ni
Amorphous ϕ	16.2	0.99	12.7	9.3	1.73	0.54
Cronstedtite	12.5	2.77	20.7	6.54	0.64	0.27
Coarse fibers	10.6	1.01	22.0	7.08	4.29	0.40
Tochilinite	1.65	0.68	30.23	1.16	19.99	2.07
Amorph, $n = 21$	1.7	0.16	2.4	1.3	0.56	0.18
Cron, $n = 31$	0.9	0.60	2.8	2.31	0.32	0.13
Coarse, $n = 17$	1.3	0.13	1.9	1.15	1.85	0.18
Toch, $n = 13$	0.99	0.21	1.78	0.53	2.15	0.43

Thermal demagnetization of SIRM shows major unblocking temperatures in the 100–200 °C range, and another minor peak in unblocking around 550–580 °C (Fig. 17b). The latter peak corresponds to magnetite. The low temperature peak can be attributed to sulfides. It is noteworthy that the FeNi phase that is visible in experiments involving magnetic susceptibility is not detectable in experiments using magnetic remanence because FeNi grains are typically a very poor carrier of remanence but have large magnetic susceptibility. The exact opposite is true for sulfides. The nature of these sulfides cannot be determined from the magnetic experiments. However, it is noteworthy that after heating to 400 °C, SIRM is basically unchanged, but has a rather different unblocking temperature spectrum, with a shift of the low temperature peak from 100–200 °C to 300–350 °C. This suggests growth of pyrrhotite, possibly from S in PCP, or possibly due to shrinkage of the pentlandite stability field.

Determining the modal abundances of each of these phases is not straightforward as their magnetic properties strongly depend on grain size. However, the average saturation magnetization (M_S) of 5.10 $Am^2 kg^{-1}$ for Paris, compared to the Ms for metal (218 $Am^2 kg^{-1}$) and magnetite

Table 10
Compositions of refractory metal nuggets (wt.%, limit of detection 0.5%).

	Re	Os	W	Ir	Mo	Ru	Pt	Rh
4 (2)		8.39	3.4	7.03	42.16	26.88	12.17	
7 (1)		18.96	4.54	5.92	38.83	20.5	8.43	1.67
		10.9		12.07	22.56	16.21	28.9	4.34
7 (1) (7-III-2)				10.25			49.64	
7 (IV I) (7-5)		11.29		14.71			74	
7 (IV-2)		13		15.6			71.4	
8-I-1 (8 (1))		18.09	1.42	16.2	13.5	19.41	11.86	3.03
8(II-1) largest RMN	1.52	21.93	1.95	21.55	4.43	21.79	0.11	2.09
(8 (3))		26.35	3.84	26.89	2.89	20.8		1.47
8-II-2 (8-4)	0.74	23.02	1.86	20.76	9.88	13.58	1.28	1.35
8-VI-1 (8-4')		8.79	1.14	9.43	15.29	14.05	25.73	1.19
8-XI-1 (8-2')	0.93	26.29	3.53	24.53	11.82	11.84	6.5	0.84
6-I-1		21.46	0.76	25.35	18.59	29.74	1.19	
		25.35		27.46	23.48	20.31		
		29.46		27.11	13.52	21.6		1.52
6-I-2	1.47	26.43	2.28	25.4	17.42	24.33	1.74	0.92
	0.53	24.44	2.76	25.34	17.06	23.9	4.58	1.42
	0.57	15.24	3.07	20.82	25.92	22.95	8.27	3.13
		23.66	1.7	24.12	16.83	27.3	4.3	1.95
6-I-3	0.87	27.34	2.66	27.81	15.25	23.3	0.53	2.22
		23.38		27.9	17.71	30.54		
		19.27	3.38	23.01	17.71	26.75		4.3
		11.03		20.43	30.05	25.87	6.87	3.46
6-VII-1		4.54	0.79	6.43	13.31	15.9	32.88	2.54
2.5.2	2.96	47.36	6.5	37.22	3.32	0.54	0.001	0.001
	1.42	34.73	3.7	32.16	8.44	16.55	0.001	0.81
		41.84	4.45	37.17	1.28		2.16	0.001
2.5-4	2.24	40.27	3.96	41.15	8.6	2.31	0.001	0.001

(102 $Am^2 kg^{-1}$) indicates a maximum magnetite content of 6.4 wt.%, and a maximum metal content of 2.7 wt.%. The amount of pyrrhotite cannot be assessed in the same way because it has much lower Ms and susceptibility. But in view of the fraction of the SIRM that is demagnetized below 350 °C (Curie temperature of pyrrhotite), and using a hypothetical $M_{RS}/M_S = 0.3$ for pyrrhotite, a maximum content of about 2 wt.% pyrrhotite can be estimated. The hysteresis parameters, with $B_{CR}/B_C = 11.6$ and $M_{RS}/M_S = 2.73 \times 10^{-2}$, indicate an overall multidomain behav-

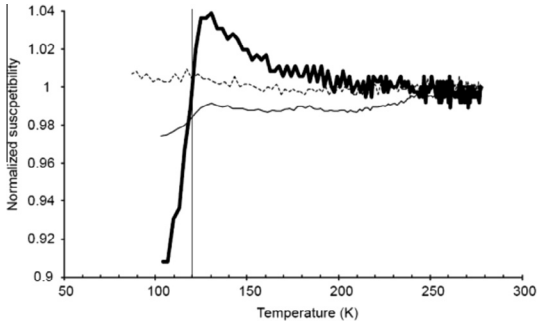

Fig. 15. Magnetic susceptibility as a function of temperature for three representative low temperature experiments: regular sample (solid line), aqueously altered sample (thick solid line), and non aqueously altered sample (dotted line). The Verwey transition temperature at 120 K is indicated by a vertical line.

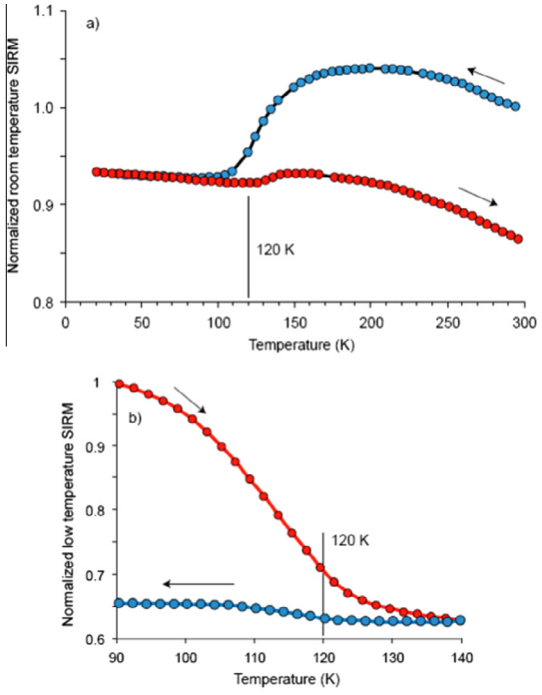

Fig. 16. (a) Low temperature cycling of room temperature SIRM for a 54 mg sample of Paris. (b) Thermal evolution of low temperature SIRM for a 155 mg sample of Paris.

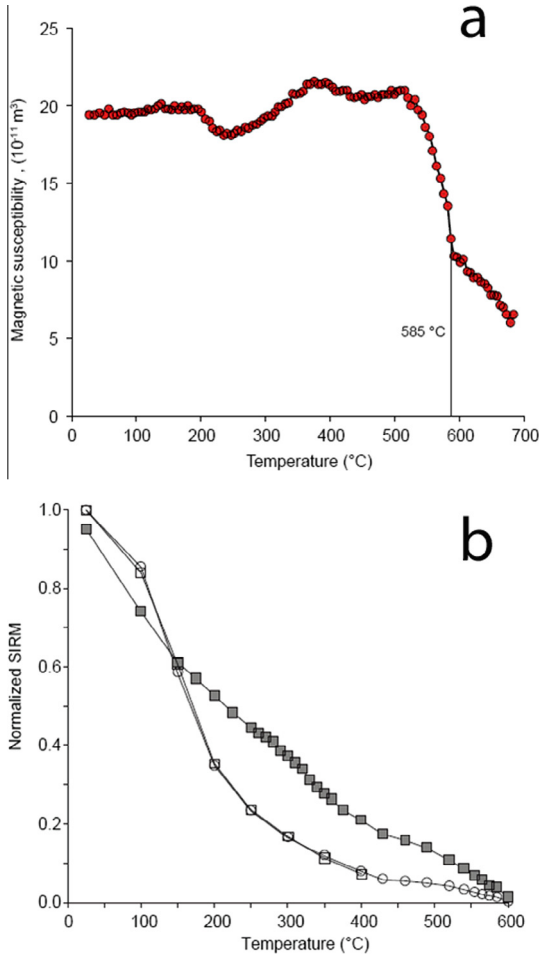

Fig. 17. (a) Magnetic susceptibility as a function of temperature for a 11 mg sample of Paris. (b) Thermal demagnetization of SIRM of two Paris samples with masses 94 mg (circles) and 40 mg (open boxes). The smaller sample was resaturated after the 400 °C heating step, and thermally demagnetized again (solid boxes).

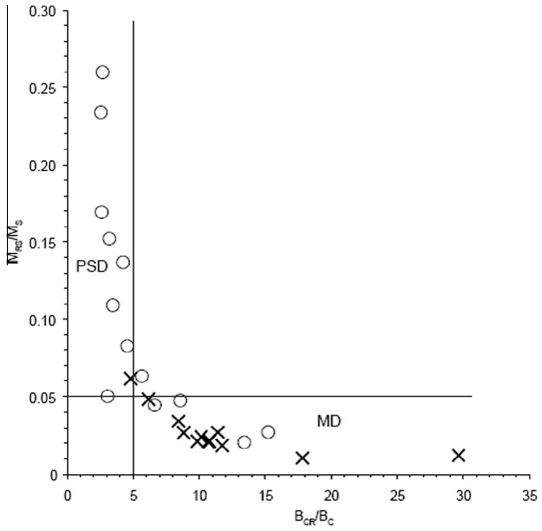

Fig. 18. Hysteresis properties of thirteen Paris samples (crosses), and thirteen samples from eight other meteorite falls (circles). The limits of the pseudo-single domain (PSD) and multidomain (MD) behaviors are indicated.

ior. This multidomain behavior is typical of multidomain FeNi grains (i.e. with grain size >100 nm). The grain size of the other magnetic phases (magnetite and pyrrhotite) is difficult to assess precisely because of mixture of three ferromagnetic minerals with contrasted magnetic properties. But by analogy with other CM chondrites it is likely in the pseudo-single domain area, indicating grain size in the 20–280 nm range for magnetite (Dunlop and Özdemir, 1997), and below 1.5 μm for pyrrhotite (Menyeh and O'Reilly, 1991), though larger grains could also be present. Magnetite of this size was not observed in our BSE images, but was found with tochilinite in some FIB sections of altered metal.

The hysteresis properties of Paris are significantly different from other CM. Saturation magnetization of Paris (5.85 Am^2/kg) is the highest among all CM falls, and is more than five times higher than the mean M_S for falls ($M_S = 0.107 \pm 0.46$ Am^2/kg measured on six CM falls (our unpublished data). This cannot be entirely attributed to a larger proportion of metal vs. magnetite (metal has an intrinsic Ms that is about only 2.4 times higher than magnetite), but also indicates a larger modal abundance of metal + magnetite in Paris than in other CM chondrites. Compared to most other CM falls, Paris has hysteresis properties that are in the pseudo-single domain area (Fig. 18). Rather than a different grain size for magnetic minerals, this is indicative of a larger proportion in Paris of metallic FeNi vs. magnetite and sulfides. It is noteworthy that despite having a larger M_S, the saturation remanent magnetization of Paris ($M_{RS} = 0.13 \pm 0.02$ Am^2/kg, measured on 13 samples), that is dominated by sulfides and magnetite to a lesser extent, is equal to the mean value for other CM falls ($M_{RS} = 0.12 \pm 0.07$ Am^2/kg, measured on 13 meteorites from 8 different falls, our unpublished data). This suggests that the modal abundance of sulfides in Paris is about the same as in other CM falls.

To summarize, Paris has a magnetic mineralogy that is homogeneous down to the scale of about 2 g. It contains magnetite, FeNi metal, as well as poorly crystalline sulfides. The less aqueously altered lithology of Paris does not contain magnetite. The most striking difference with other CM chondrites is the significantly higher amount of FeNi metal in Paris, estimated at 2.7 wt.% in the least aqueously altered lithology. This higher amount cannot be entirely explained by a lower degree of aqueous alteration of metal in Paris, and also implies a higher total modal abundance of metal + magnetite in Paris than in other CM chondrites, probably related to the higher ratio of chondrules to matrix.

4.4. Carbon

In our TEM work, we observed that organic globules are common in the Paris matrix (Fig. 10b). Other authors have reported on organic material in Paris. A separate section (SPSR-1), prepared for Remusat et al. (2011) with-

out using epoxy, was studied by NanoSIMS using rastering of a focused Cs + beam to generate secondary ion images of H^-, D^-, $^{12}C^-$, $^{16}O^-$, $^{26}CN^-$, $^{28}Si^-$ and $^{32}S^-$ in micron sized organic particles. C/H ratios in matrix IOM appear significantly lower than in other CM chondrites (Remusat et al., 2011). The D/H ratio in more and less altered regions is indistinguishable. A few D-rich hot spots are observed, with a maximum at $\delta D = 7950 \pm 330‰$, suggest that aqueous alteration on the CM parent body does not induce a significant modification of the composition of organic particles (Remusat et al., 2011).

Crushed fragments weighing a few mg were used by Merouane et al. (2012) for mid and far IR and Raman micro-spectroscopy. Some IR spectra of aromatic-rich micron-sized fragments of Paris resemble those of other CM chondrites, but others match spectra in the 3.4 and 6 μm regions for organics from the diffuse interstellar medium (Merouane et al., 2012). They find a CH_2/CH_3 ratio of 2.2 ± 0.2 in agreement with the value for ISM objects. The good match for the spectra suggests that Paris may have preserved some organic matter of interstellar origin.

5. PETROLOGY OF HIGH TEMPERATURE COMPONENTS

5.1. Refractory Inclusions

Ninety five refractory inclusions (RI), of size ~100–200 μm, were identified using BSE in the thin section 2008 LM, making up ~0.4% by area of the 4.5 cm^2 section. Phases in CAI were identified from EDS spectra and semi-quantitative analyses on the Tescan VEGA SEM sufficient to define stoichiometry. The CAI are mainly fine-grained spinel-rich inclusions. The occurrence of forsterite rims on some CAI and of small nodules of CAI inside some AOA demonstrates their kinship. The AOA are porous and frequently fractured, with most grains ~1–5 μm long (Fig. 19a). In addition to forsterite, they may contain kamacite and/or orthopyroxene. Their CAI minerals include spinel and fassaite, while alteration is mainly to cronstedtite with some tochilinite.

Spinel is a major mineral in CAI and it occurs as nodules, either massive or containing more refractory phases. The sequence hibonite, perovskite and grossite is observed encased in spinel in inclusion 268 (thin section 2008 LM), and spinel is mantled by gehlenite, followed by anorthite, followed by diopside (Fig. 19b). Hibonite is zoned to Ti–Mg-rich rims. The sequence spinel followed by gehlenite is common in CM chondrites, though not predicted by the equilibrium condensation sequence (Simon et al., 2006). Rarely there are small inclusions of gehlenite in spinel in inclusion 268. These are possibly protrusions of the mantle into the plane of the section, but they might also be evidence that some gehlenite managed to nucleate on and replace spinel, as in rare cases reported by Simon et al. (2006).

Other CAI contain fewer phases, but with the same formation sequence. Perovskite or hibonite may be the only phase earlier than spinel, or there may be no phases earlier than spinel. Gehlenite and anorthite are not common in other Paris CAI. The vuggy inclusion 285 (thin section 2008 LM) consists almost entirely of hibonite laths (Fig. 19c), but hibonite is coated with spinel, which is followed in turn by fassaite, in interior cavities, (Fig. 19d). Kamacite (3–4% Ni) is present in a few inclusions, mantled like spinel by diopside or occurring between fassaite and the outer mantle of forsterite.

Other Paris sections contain similar RI but we observed one distinctive and very large (about 800 μm) zoned inclusion in section 2010-05. Perovskite appears to have been the first phase to form in this CAI, which is spinel-rich throughout. It has a central region where perovskite and lathy or ragged spinel are encased in massive gehlenite (Fig. 19e). This region is surrounded by a highly porous region lacking gehlenite but with the same lathy spinel (Fig. 19f), which grades outwards into a region where the matrix is a silicate rich in O, Al and Na, i.e. with a zeolite-like composition, and with minor S and Cl. This CAI thus appears to record the partial dissolution and replacement of melilite. In the outer part of the altered mantle, the spinel is more equigranular and is partly mantled by ~1 μm of a Ca–Ti–Al–Mg-rich silicate, probably fassaitic pyroxene. The whole is encased in a rim of diopside/fassaite 10–25 μm thick, locally forming extensions containing spinel-rich nodules, in turn surrounded by a serpentine-rich mantle.

The simplest CAI contain spinel mantled by diopside or fassaite, with an outer rim of forsterite in many cases (Fig. 20a) and many of them show no alteration. The main alteration seen in CAI is formation of cronstedtite between spinel and pyroxene (Fig. 20b). We note that this horizon corresponds to gehlenite, where present, and which is replaced by void space and a zeolite-like Na–Al silicate in the large CAI 2010-05-01. Calcite and an Mg-rich, Al-bearing phase with elevated oxygen, probably a hydroxide, are found in heavily altered inclusions.

Magnetic and density separates were prepared after using the freeze–thaw method on Paris. Hibonite-rich objects were handpicked at IPGP from these fractions for SIMS analysis. Mg isotopes of 14 spinel-hibonite spherules (SHIBs) and one platy hibonite inclusion (PLACs), ~30–40 μm in size in most cases, were analyzed by Liu et al. (2012), along with samples from the Murchison CM chondrite. Mg isotopic data for SHIBs show heterogeneity and suggest formation with gradually increasing $^{26}Al/^{27}Al$ to roughly the canonical level in the solar nebula. The maximum value for $^{26}Al/^{27}Al$, 6×10^{-5} suggests that SHIBs predated CAIs (Liu et al., 2012). Platy hibonite has no clear excess in ^{26}Mg and may have formed before the injection of ^{26}Al into the disk. Liu et al. (2012) concluded that hibonite formed in the first few thousand of years of Solar System history.

Refractory Metal Nuggets (RMN) have been identified in the BSE mode (Tescan SEM, MNHN) during systematic traversing of polished thin sections at magnification 500×. RMN occur exclusively inside CAI or attached to disrupted CAI minerals. RMN-bearing CAI (13 in all) were investigated with the SEM in five polished sections and were found in all of them. Their abundance, size and compositions vary as a function of host CAI minerals. RMN in

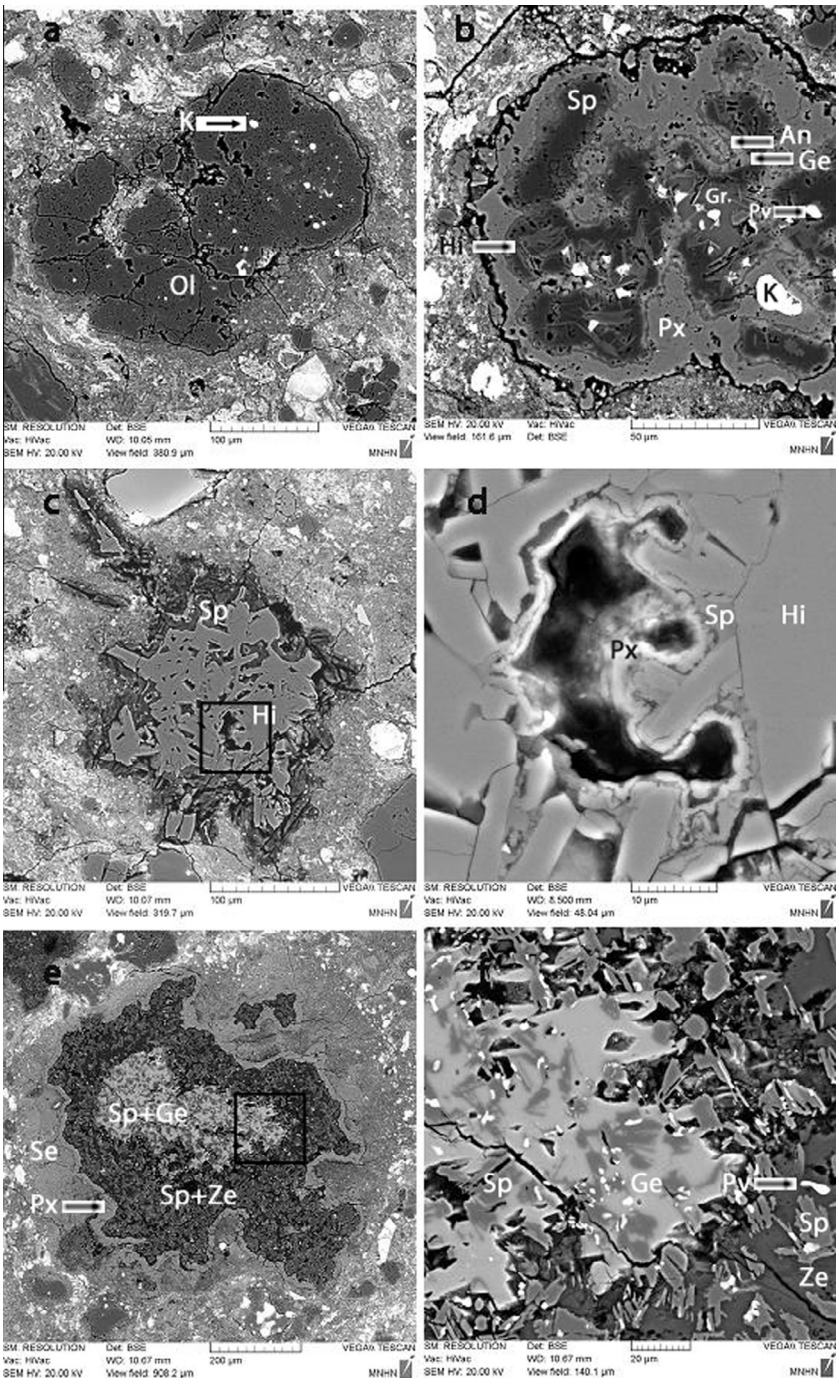

Fig. 19. BSE images of refractory inclusions in Paris 2008 LM (a–d), and Paris 2010-05 (e–f). (a) amoeboid olivine aggregate containing forsterite and kamacite. (b) CAI 268 contains nodules of spinel (darkest grey, except for black pores); the sequence hibonite (medium grey needles), perovskite (white) and grossite (medium grey) is mantled by the spinel; the sequence gehlenite (light grey), followed by anorthite (medium grey), followed by diopside/fassaite (medium grey) mantles the spinel nodules; the large kamacite grain (white) is also embedded in the diopside. (c) CAI 285 consists almost entirely of hibonite laths, with spinel on the exterior. (d) CAI 285 is vuggy (detail of (c)), with hibonite laths coated by spinel (medium dark grey), followed in turn by fassaite (very light grey), in interior cavities. (e) CAI 2010-05-01 is a zoned spinel-rich inclusion about 800 μm long, in which perovskite was the first phase to form. In the center perovskite and lathy or ragged spinel are encased in massive gehlenite. The surrounding region is porous with no gehlenite and grades outwards into a zeolite-like region encased in a rim of diopside/fassaite 10–25 μm thick, surrounded by a serpentine-rich mantle. (f) CAI 2010-05-01: close-up of transition from gehlenite-rich to porous to zeolite-like, with spinel in all three. Symbols: Ol forsterite, Px diopside or fassaite, K kamacite, Hi hibonite, Pv perovskite, Gr grossite, Sp spinel, Ge gehlenite, An anorthite, Ze zeolite-like phase, Se serpentine.

Fig. 20. BSE images of CAI. (a) CAI 257 is a typical fine-grained spinel-rich CAI. There are diopside rims around spinel, and an incomplete fine rim of forsterite (Paris 2008 LM). (b) Altered fine-grained spinel-rich CAI 258. Perovskite inclusions in spinel, rim of cronstedtite (bright grey) and incomplete outer rim of fassaite (Paris 2008 LM). (c) The largest RMN-bearing CAI with tens of evenly distributed submicron RMN which occur preferentially in Y-rich perovskite phase (Paris 2010-6). Symbols: Ol forsterite, Px diopside or fassaite, K kamacite, Pv perovskite, Sp spinel, Cr cronstedtite.

the two most refractory CAIs (containing hibonite, Paris sub-sample 2.5, and Y-rich perovskite + Al spinel, Paris 2010-6) are very small-size inclusions (a few tens of nanometers to less than 500 nm). They form clusters of several inclusions inside hibonite. The largest RMN-bearing CAI yet discovered in Paris meteorite appears to be dotted with tens of evenly distributed, small (100 nm to less than 1 μm in maximum dimension) individual RMN which preferentially occur in the Y-rich perovskite phase (Fig. 20c). RMN in spinel-perovskite (Y-free) CAI are isolated grains (1–3 per CAI) preferentially included in spinel. These are larger (ca. 500 nm to 1 μm) RMN cuboids, with cubo-octahedral or hexagonal cross-section. Isolated RMN grains have also been identified in Al-spinel + Ca–Al pyroxene CAIs and Al-spinel coexisting with forsterite. The largest RMN (2.5 μm) is included in forsterite.

Semiquantitative chemical compositions were determined with the SEM on the largest RMN particles using a standardless EDX procedure (Fig. 21, Table 10). The most refractory alloys occur in the hibonite grain (Paris 4039 2.5), with compositions dominated by Os (47.4) and Ir (37.2), coupled with the highest Re (3.0) and W contents (6.5 wt.%). The RMN analyzed in perovskite + Al-spinel CAI are Os–Ir–Mo–Ru alloys containing detectable amounts of Re (up to 1.5 wt.%) and W (up to 3.3 wt.%), coupled with low contents of the less refractory PGE (<8 wt.% Pt). Those hosted in spinel (i.e. remote from perovskite) are enriched in Pt (up to 29 wt.%) and Rh. RMN enclosed in forsterite are Pt–Fe-rich alloys.

Refractory metal nuggets akin to those reported from the Paris meteorite were extensively documented in CM2 (Murchison; Berg et al., 2009; Schwander et al., 2011, 2012; Harries et al., 2012; Croat et al., 2013), CV3 (Allende, Palme and Wlotzka, 1976; Blander et al., 1980; Schwander et al., 2013; NWA 1934, Leoville; Schwander et al., 2013), and very recently, in a quite different petrological setting however (low-density fraction in presolar graphite grains, CI (Orgueil-like) chondrites, Croat et al., 2013). Enriched in refractory siderophile elements by 5–7 orders of magnitude over the CI abundances, RMN match compositions of early nebular condensates (Palme and Wlotzka, 1976); their compositions are reproduced by chemical equilibrium calculations of high temperature condensation into hcp single-phase alloys (Harries et al., 2012) from a cooling gas of solar composition. In Murchison, RMN were thought to have been once residing in CAIs, but relationships with CAI's mineral assemblages were lost because all studies were performed on acid-resistant concentrates (Berg et al., 2009; Harries et al., 2012; Schwander et al., 2012). Murchison and Paris show strikingly similar features, regarding size (20 nm–1.3 μm), the regular shape of RMN particles and their compositional range (7–57 wt.% Os vs. 8–47 wt.%), in spite of the higher number of analysed grains in Murchison (>100 vs. 25 for in Paris). The polyhedral surface faces indicate growth in a gas phase. Empirical calculation from condensation models indicates a wide range of condensation temperatures for such alloy compositions, from ca. 1600 K to less than 1450 K, similar in both meteorites. Berg et al. (2009) for Murchison assumed the highest condensation T to be similar to that of perovskite; in Paris

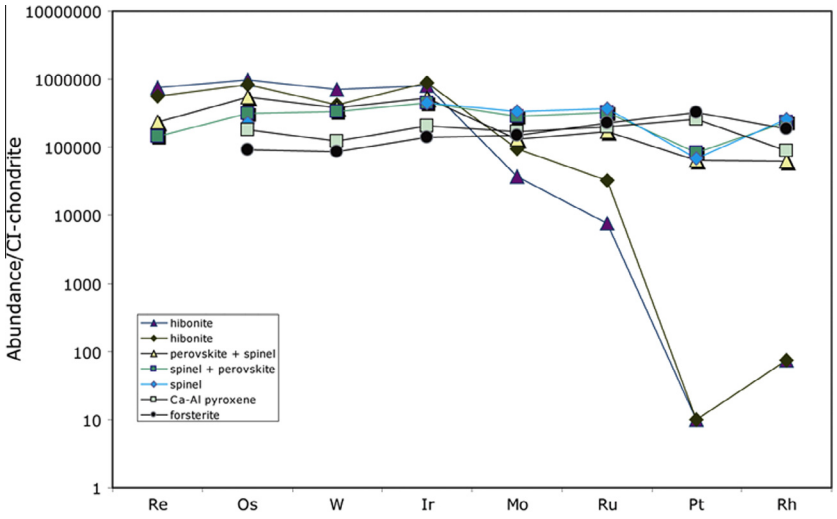

Fig. 21. Chondrite-normalized compositions of RMN in Paris CAI. Refractory siderophile elements decrease following the observed condensation sequence of the host oxide and silicate phases.

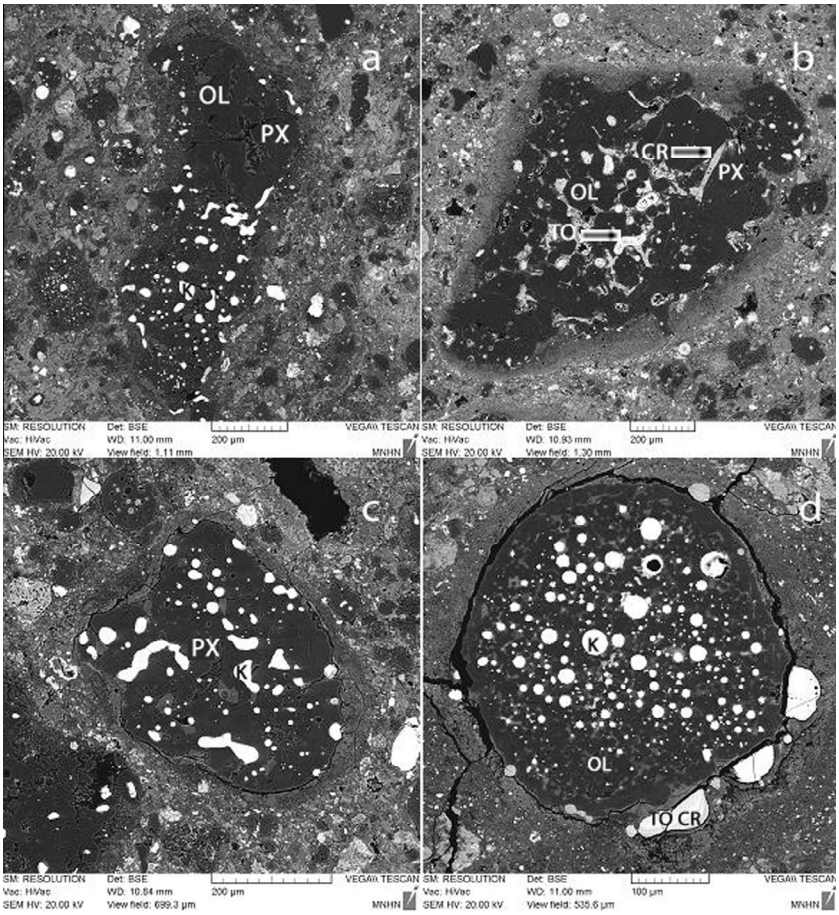

Fig. 22. BSE images of metal-rich Type I chondrules in Paris 2010-04, -06 and -07. (a) Chondrule 2010-07-6 is a Type IABm with kamacite (5.4% Ni, 0.5% P, 0.8% Cr), olivine $Fa_{0.6–0.9}$ and pyroxene $Fs_{0.9–1.3}Wo_{1.0–2.3}$; the mesostasis contains diopside. (b) 2010-07-11 is a Type IABm chondrule with $Fo_{1.0–2.0}$. In the central porphyritic zone, metal replaced mainly by tochilinite is in contact with mesostasis altered mainly to cronstedtite. Metal inside olivine is fresh. Pyroxene in the poikilitic mantle is etched. (c) 2010-07-2 is a Type IBm chondrule with kamacite (5.4% Ni; 0.5% P, 0.6% Cr) and pyroxene $En_{1.0–6.7}Wo_{0.7–1.0}$ plus minor diopside. (d) 2010-04-6, containing metal droplets up to 35 μm in diameter with 2.95 wt.% Si. The growths on the surface of the chondrule contain cronstedtite and tochilinite. Symbols: OL forsterite, PX diopside, K kamacite, TO tochilinite, CR cronstedtite.

(Fig. 21), the most refractory RMN are hosted in hibonite. Moreover, Fig. 21 shows that abundances of the most refractory PGE decrease following the observed condensation of the host oxide and silicate phases of RMN. This relationship adds further evidence for a nebular condensate origin; RMN served as nucleation centres for host silicates and oxides.

RMN in the Paris chondrite escaped significant alteration prior to incorporation into their parent body. There is no sign of significant W and Mo depletion in Paris and Murchison RMNs, in contrast to Allende CAIs that show strong depletion in those easily oxidized and sulfurized elements (e.g. Palme et al., 1994; Schwander et al., 2013). Alteration by parent body processes is limited to a few Pt–Ir-rich alloys redistributed in Fe–Ni sulfides; similar assemblages were documented in R chondrites (Schulze, 2007). However, Paris is devoid of the As-, Sn-bearing noble metal minerals that testify to extensive parent body alteration in R chondrites.

5.2. Type I chondrules

Type I chondrules in Paris are approximately 48% Type IA (PO), 39% Type IAB (POP, mostly metal-rich) and 13% type IB (PP). Metal-rich Type IAB (Fig. 22a) and metal-rich Type IB (Fig. 22 c) are conspicuous in the freshest zones, but can also be recognized easily when the metal is pseudomorphed by alteration minerals (Fig. 22b). Mesostasis is not very abundant so that the textures are more granular than strictly porphyritic, except in chondrule centers where mesostasis is concentrated. Dusty (metal-bearing) relict grains were not observed. Glass is replaced by phyllosilicates, whereas olivine, pyroxene and metal are generally unaltered. In the more altered regions, metal in Type I chondrules may be replaced by tochilinite and related minerals, especially if in contact with mesostasis (Fig. 25c).

Histograms of olivine and pyroxene compositions in 54 Type I chondrules are given in Fig. 23. Mean compositions of olivine and pyroxene are $Fa_{0.9}$, s.d. 0.7 and $Fs_{2.3}Wo_{1.4}$, s.d. 1.7 and 1.3, respectively. Diopside or fassaite occurs in the mesostases of some of these chondrules. Diopside in some cases contains exsolved pigeonite, with exsolved lamellae on (0 0 1) ~10 nm wide. Ca decreases and Cr increases sharply in olivine going from Fa_0 to Fa_1 (Fig. 24).

Metal in Type I chondrules and isolated globules in matrix is on average chondritic in Ni/Co and in Ni/P, with a small range of Ni, mostly ~4 to ~8 wt.% but some up to 12 wt.%, and scatter of Co (0–0.7 wt.%) and P (Fig. 25a and b) related to exsolution. Subsets of the metal analyses have very high and very low P concentrations, consistent with the observed exsolution of P-rich phases.

Metal grains in matrix and Type I chondrules may contain inclusions of other phases. Those with low concentrations of dissolved Si contain small inclusions (Fig. 8d), mainly tabular 100 nm–1 μm inclusions, of an SiO_2 polymorph with a common alignment (Bourot-Denise et al., 2010). These fine inclusions tend to be near the edge of the grains and not in their centers, possibly due to zoning in Si or to limited diffusion of O into the metal. Cristobalite

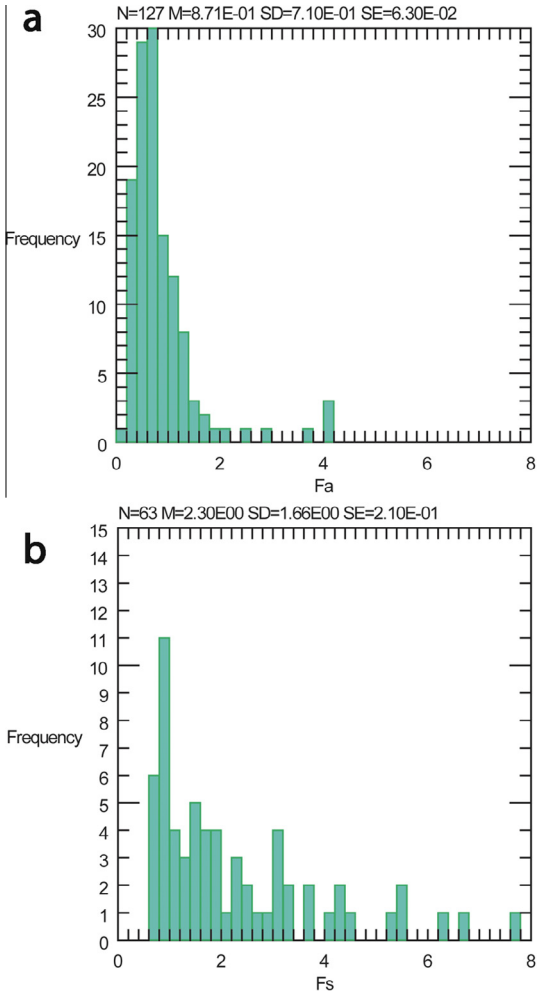

Fig. 23. Histograms of olivine and pyroxene compositions in Type I chondrules.

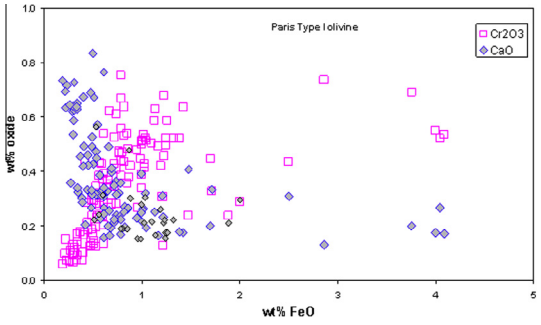

Fig. 24. Variation of Ca and Cr concentrations of forsteritic olivine in Type I chondrules.

and silica glass inclusions were identified in metal by Caillet Komorowski et al. (2011). The crystallographic alignment (Fig. 19d) indicates an origin by exsolution as negative crystals. Inclusions of daubréelite, Cr phosphide, chromite, schreibersite and troilite were also observed in metal (Bourot-Denise et al., 2010). Assemblages of several of

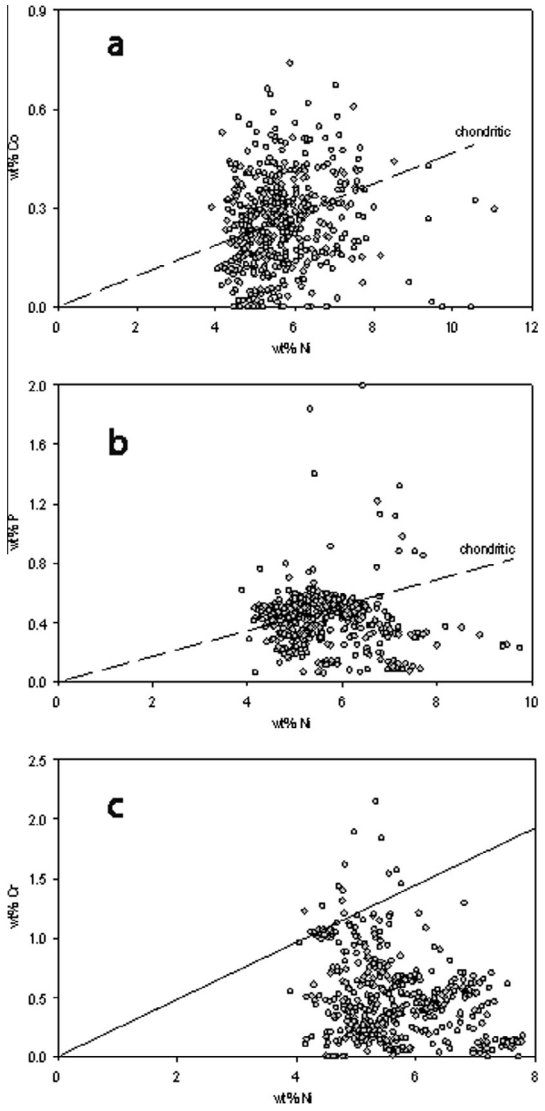

Fig. 25. Metal compositions: Ni vs. (a) Co (b) P (c) Cr. Metal in Type I chondrules and isolated globules in matrix is generally chondritic but Cr varies from chondritic to highly depleted due to oxidation in the chondrules.

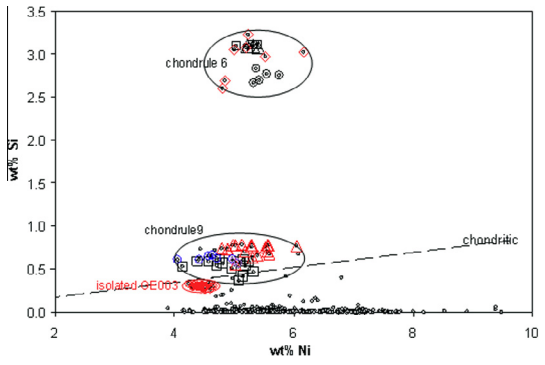

Fig. 26. Metal in Type I chondrules and in matrix in section 2010-04 is generally poor in dissolved Si, but is Si-rich in chondrules-9 and -6, and in matrix grain 3. Different symbols are used to distinguish different metal grains in the same chondrule. Chondrule 2010-04-6 is shown in Fig. 21.

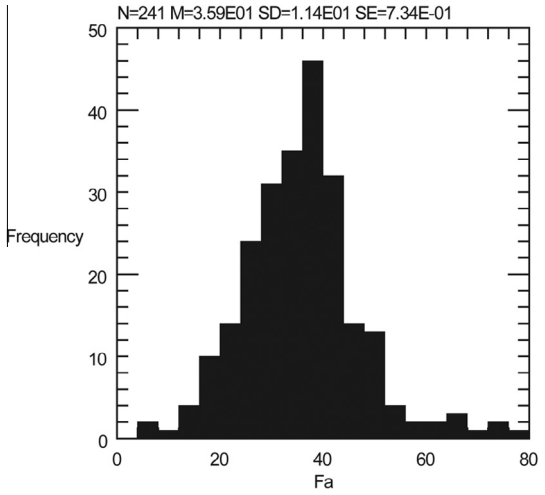

Fig. 27. Histogram of compositions of olivine in Type II chondrules.

these phases were found near the exteriors of the same metal grains.

However, unlike the other elements in metal, Cr concentrations are mostly highly depleted relative to Ni (Fig. 25c), Co and P. A correlation of Fa vs. "Cr_2O_3" in the most forsteritic olivine ($Fa_{0.2\ to\ \sim1}$) and a negative correlation between Cr in metal and Cr_2O_3 in olivine indicates that most of this variation is due to oxidation: metal and silicate equilibrated during crystallization of chondrules (Zanda et al., 1994). However the lowest Cr concentrations (<1% Cr) are associated with very low P concentrations, and are due to exclusion of Cr phosphide precipitates from the analyzed regions. The calculated fO_2 for the OIP buffer assemblage and for Cr partitioning between metal and olivine or pyroxene (Kring, 1986; Zanda et al., 1994) is $\sim10^{-11}$ at 1600 °C (IW-3).

Si concentrations, with exceptions, are close to EMP detection limits (Fig. 26). We found two chondrules in which metal contains 2.95% Si, s.d. 0.19, and 0.64% Si, s.d. 0.11. Some isolated metal droplets in matrix, like grain 3 in Fig. 26, also have significant Si. In Fig. 26, we use different data symbols for individual metal grains in the two chondrules. Different metal grains within a given chondrule may have similar yet significantly different Si concentrations (Fig. 26). The moderately Si-rich metal in chondrule 2010-04-09 occurs as 50–100 μm droplets. The exceptionally Si-rich metal in chondrule 2010-04-06 occurs as numerous small spheres, from ~35 to a few microns in diameter (Fig 22d), with irregular boundaries as if accreting nanospherules, unlike the irregular blebs in most Type I chondrules (Fig. 22). The chondrule resembles a quenched spherule with an emulsion of two liquids. The interior metal is fresh, except very close to the edge, though there are three tochilinite–cronstedtite growths with some minute P/Cr inclusions, and also small magnetite growths on the chondrule surface. The Si-rich metal is associated with very Cr-poor silicates, yielding an fO_2 estimate from Cr partitioning of $\sim10^{-12}$ at 1600 °C (IW-4). These silicates are not more magnesian than usual, however, indicating some redox disequilibrium.

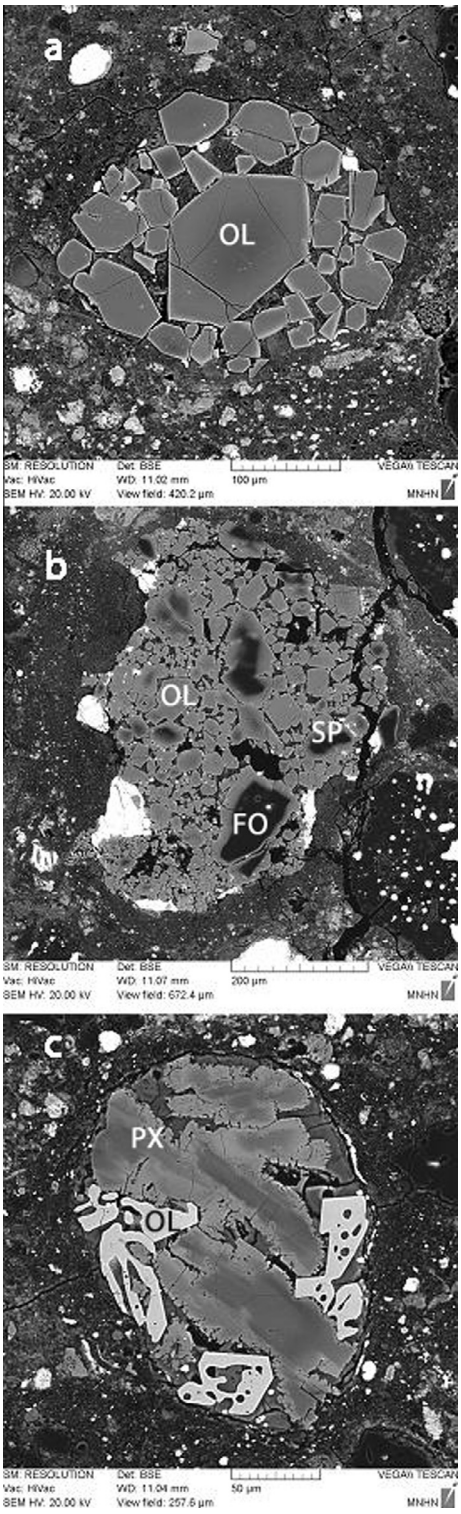

Fig. 28. BSE images of Type II chondrules in section 2010-04. (a) Type IIA PO chondrule-17 with olivine $Fa_{26–33}$. (b) Type IIA chondrule-9 with olivine $Fa_{29–40}$, numerous relict olivine grains $Fa_{1–11}$ and one relict spinel grain. (c) Type II(A)B chondrule-16 with pyroxene $Fs_{40–63}Wo_{1–6}$ and olivine (white) $Fa_{74–75}$. OL olivine, PX pyroxene, FO relict forsterite and SP relict spinel.

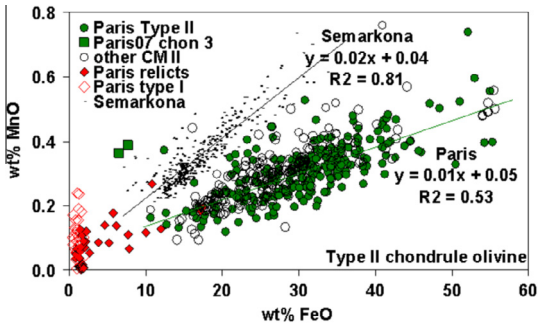

Fig. 29. FeO–MnO relations in olivine in chondrules in Paris, other CM chondrites and Semarkona. Paris Type II chondrules are typical of those in carbonaceous chondrites and unlike those in UOC. Relict grains overlap the fields between Type I and Type II chondrule olivine compositions.

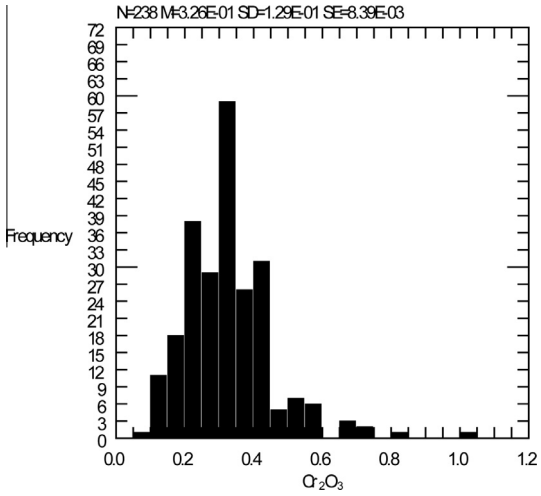

Fig. 30. Histogram of wt.% Cr_2O_3 in olivine of Type II chondrules and fragments has the form of those in 3.0 chondrites (Grossman and Brearley, 2005).

5.3. Type II chondrules

Type II chondrules and fragments make up 1–2% of Paris, and there are many tiny ferroan olivine crystal fragments. They are dominantly Type IIA (PO) chondrules, but several kinds of pyroxene-bearing Type II chondrules are present. The range of melt-grown olivine compositions is Fa_7 to Fa_{76} (Fig. 27). We have included a chondrule with Type IIA PO texture and $Fa_{7–8}$ in this histogram, though its FeO/MnO ratio shows it is intermediate between Type I and Type II olivine (Hewins and Zanda, 2012). Porphyritic olivine texture is illustrated in Fig. 28a, and ~100 μm relict forsterite grains are common in such IIA chondrules (Fig. 28b). Preliminary accounts of these chondrules have been given in Hewins et al. (2011) and Hewins and Zanda (2011). Sulfide in Type II chondrules has the stoichiometry of Canyon Diablo troilite, and up to 1% Ni. Pentlandite was also observed where sulfide is very abundant.

We made EMP analyses of 9 chondrules or chondrule fragments containing pyroxene. There are two IIAB and two IIB chondrules; two II(A)B, with minor highly ferroan olivine; and three IIA(C) with augite as the only pyroxene. In the IIAB chondrules olivine compositions are $Fa_{37–61}$ and orthopyroxene $En_{36–42}Wo_{0–2}$. One II(A)B has olivine $Fa_{32–44}$ and orthopyroxene $En_{34–38}Wo_{1}$. The II(A)B illustrated in Fig. 28c contains olivine Fa_{74} and highly zoned orthopyroxene–pigeonite $En_{40–63}Wo_{1–6}$. The augite in the IIA(C) chondrules is $Fs_{9–27}$ $Wo_{36–41}$.

Type II chondrule olivine in Paris and other CMs (Murchison, Mighei and Cold Bokkeveld) show the same FeO–MnO correlation (Fig. 29), with FeO/MnO ~100, which is similar to that for CO chondrites (Berlin et al., 2011), CV (Rubin and Wasson, 1987), Tagish Lake (Simon and Grossman, 2003; Russell et al., 2010), Acfer 094 (our data) and Wild 2 (Frank et al., 2012). This olivine has significantly higher Fe/Mn than that for chondrules from ordinary chondrites (Berlin et al., 2011; Hewins and Zanda, 2012). However for Paris there exist distinct outliers from this distribution, reflecting reservoirs different in Fe/Mn. Ferroan relict grains connect the fields for Type II and Type I chondrules (Fig. 29), and only the most forsteritic relics plot in the field for Paris Type I olivine.

Fig. 30 shows a histogram of Cr_2O_3 concentration in 238 ferroan olivine grains in Type II chondrules, chondrule fragments and isolated in Paris matrix. The distribution is very similar to those in histograms (Grossman and Brearley, 2005) for three 3.0 CO chondrites and Acfer 094, and unlike those for two slightly re-equilibrated (CO 3.2) chondrites. Olivine generally shows normal zoning for Ca, Mn and Na, but in chondrules with chromite, it is fractionated to lower Cr, reflecting the co-crystallization of chromite and olivine (Hewins et al., 2011). Reverse zoning due to reheating is not observed.

6. DISCUSSION

6.1. Degree of alteration

6.1.1. Mineralogy–petrology

The abundance of metal, amorphous material and poorly crystalline phyllosilicates in Paris indicates a low degree of alteration. The least altered areas are close to the microstructure of the Meteorite Hills MET 00426 and Queen Alexandra Range QUE 99177 CR chondrites of type 3.00 (Abreu and Brearley, 2010), and the ungrouped Acfer 094 chondrite (Greshake, 1997). These primitive chondrites also contain nanosulfides and forsterite in association with the amorphous phase, as in Paris (Figs. 9a and 11a, respectively).

Paris contains up to 3× the metal content of the least altered CM studied by Rubin et al. (2007). Metal grains in its matrix show rimming with tochilinite, a reaction during the earliest stage of CM alteration (Tomeoka and Buseck, 1985). A typical grain in a moderately altered region of section 2010-4 has a rim ~2–10 μm thick, as shown in Fig. 8c. This corresponds to alteration stage 1 of the aqueous alteration scale 0–4 of Palmer and Lauretta (2011). It indicates the beginning of replacement of metal grains by S-rich water in fresh matrix.

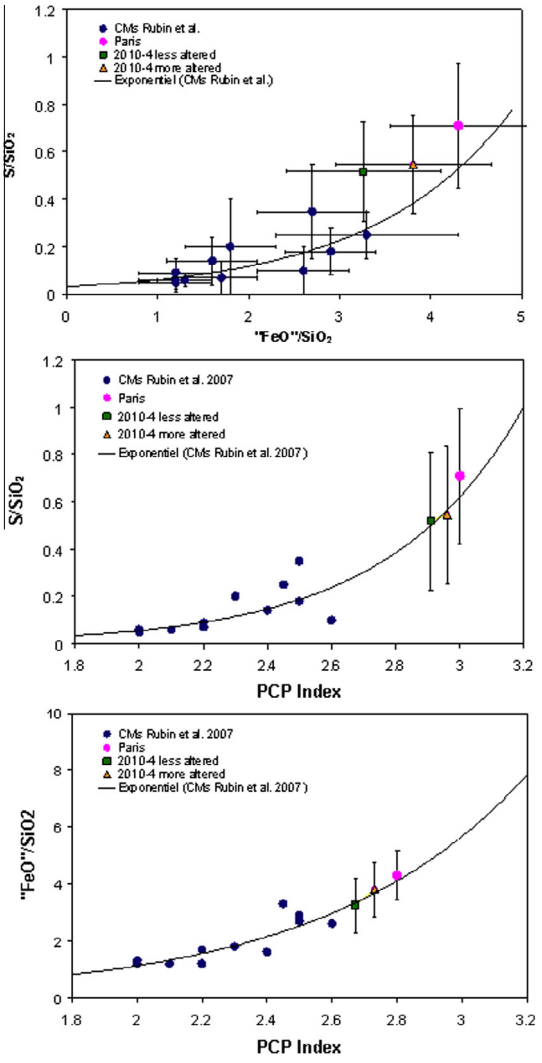

Fig. 31. (a) The PCP index for CM chondrites (Rubin et al., 2007) and Paris uses the composition of tochilinite–cronstedtite intergrowths as an estimate of petrographic type. (b and c) Paris points are placed arbitrarily to fall near the curve at 2.7–3.0. Error bars are for one standard deviation and Paris points are not significantly different. The PCP Index, designed to measure the replacement of cronstedtite, suggests that the freshest material in Paris, where little cronstedtite has grown, is more altered than bulk.

Phyllosilicates and tochilinite are abundant in more altered regions of the meteorite, and the microstructure is like those of other CM chondrites (e.g. Tomeoka and Buseck, 1985; Lauretta et al., 2000). In these CM chondrites, alteration is seen to involve the formation of serpentine (chrysotile–greenalite solid solution) from Fe-rich phases, including cronstedtite, and little Fe metal has survived (Tomeoka and Buseck, 1985; Browning et al., 1996; Rubin et al., 2007). Several measures of degree of alteration attempt to quantify the degree of serpentine formation. Browning et al. (1996) used the Fe^{3+}/Si ratio in fine matrix to reflect the replacement of cronstedtite but phyllosilicates in Paris contain too many inclusions, mainly of sulfide, for this approach to be reliable. This in itself indicates the

immature, unequilibrated nature of its aqueous alteration phases (Palmer and Lauretta, 2011).

Rubin et al. (2007) devised a composite index to CM alteration, tracking metal abundance, alteration of chondrule phenocrysts, and in which the composition of PCP aggregates plays an important role. The petrologic (alteration) subtypes defined range from 2.6 (moderately altered) to 2.0 (totally altered). Rubin et al. (2007) showed that this sequence correlated with decreasing S/SiO_2 and $\sum FeO/SiO_2$ in PCP, i.e. the approach to a simple serpentine composition. We attempted to use these composition relations to define the petrologic subtype of Paris. Many tochilinite-rich intergrowths were excluded because they have less than the 10% necessary for the PCP index. We show the compositions of Paris and CM PCP in Fig. 31a. We used exponential fits to the composition-index data of Rubin et al. (2007) as linear regressions placed Paris at values greater than the desired limit of 3.0. Paris falls on the "FeO"/SiO_2 curve near subtype 2.8 (Fig. 31b) and on the S/SiO2 curve near 3.0 (Fig. 31c). Blanchard et al. (2011) reported similar compositions of PCP in Paris sections 2010-5 and -7.

We also used the PCP Index in an attempt to distinguish the less and more altered zones of section 2010-04, domains ~1 cm in size (Fig. 6, 7a). Very few PCP analyses in the fresher zone were suitable as they were too poor in SiO_2 and cronstedtite, probably because PCP had not evolved as much as in 2.6 CM chondrites. The data showed that the fresh zone had a lower petrographic index than the more altered zone (though not statistically significant), because cronstedtite is more abundant in the more altered zone than in the fresh zone, not less as for the most altered "normal" CM chondrites for which the PCP index was developed by Rubin et al. (2007).

Based on PCP intergrowths in bulk Paris, it would be classified as an alteration subtype 2.9 ± 0.1. This PCP index suggests very little replacement of primary matrix silicates, and the presence of amorphous or poorly crystalline phyllosilicates reinforces a low alteration index. A complication in the PCP index approach is that in the earliest stages of alteration, tochilinite and cronstedtite may form from amorphous matrix material and metal. We are studying the evidence for an early increase rather than a decrease in cronstedtite abundance in the less altered regions of Paris (Leroux et al., 2013). Parent body alteration in CM chondrites probably occurred as a water-limited process and there are substantial variations in alteration within short distances in other CM chondrites too (Brearley, 2006; Palmer, 2009). The local abundance of metal and the amorphous phase in Paris suggests low ice contents with a heterogeneous distribution.

6.1.2. Bulk chemical and oxygen isotopic composition

Fresh and altered matrix differ in composition. LA-ICP-MS data (Fig. 4) for altered matrix exhibits a volatile-depleted pattern characteristic of CM chondrites, but matrix in unaltered regions has undepleted abundances like CI chondrite (Zanda et al., 2011a,b). These results are compatible with an origin for carbonaceous chondrites by mixing the high temperature fraction with CI dust (Grossman and Olsen, 1974; Wolf et al., 1980), with subsequent modification during aqueous alteration. Importantly, the effect of aqueous alteration is seen in Paris to facilitate elemental transport on the millimeter scale between the original matrix and refractory material, so that fine-grained regions petrographically identifiable as altered matrix are now similar in composition to the bulk CM.

The work of Clayton and Mayeda (1999) has demonstrated that significant oxygen isotopic differences exist between the composition of CM2 whole rocks and matrix separates. Thus, Murchison has a whole rock $\delta^{18}O$ composition of 7.30‰, whereas the matrix has a significantly heavier value of 12.7‰. However, in view of the relatively uniform modal content of Paris (~47% chondrules) the 4.5‰ difference between the least and most altered portions of the meteorite cannot be explained on the basis of modal matrix variations. Instead oxygen isotope variation can be explained by local-scale differences in the extent of alteration. For the variations in Fig. 6, this reflects variation in fluid rock ratios, but for heavily altered clast (Fig. 7b) there could have been a longer duration of alteration.

As is clear from Fig. 2b analyses from Paris significantly extend the CM2 oxygen isotope trend towards the CO3s, although a distinct gap still exists between the two groups. This suggests that, while the anhydrous precursor to the CM2s was CO3-like, the two groups are samples from distinct asteroidal sources. The main difference between the two groups was presumably the content of ice/water that accreted into their respective parent asteroids, with the CO3 being essentially anhydrous and the CM2s ice/water rich. The evidence from dark inclusions (Zolensky et al., 1993) suggests that CM2-like material was widespread in the early Solar System and consequently the existence of multiple CM parent bodies cannot be ruled out. However, the oxygen isotope data from Paris and other CM2s suggests that if there were a large number of such bodies then they all experienced a remarkably similar style of aqueous alteration.

6.2. Thermal history

6.2.1. Olivine and chromite

The distribution of Cr in olivine and its relationship to primary spinel or exsolved chromite are guides to metamorphic history (Engi, 1983; Johnson and Prinz, 1991; Grossman and Brearley, 2005). Mild reheating causes precipitation of chromite in Cr-bearing igneous olivine. Grossman and Brearley (2005) recommended study of Cr in olivine with >~2% Fa, but since olivine Fa_{2-10} is rare in Paris, we applied their approach to Type II olivine. The mean and standard deviation of Cr_2O_3 concentrations in Paris olivine are 0.33 and 0.13 wt.% Cr_2O_3, respectively lower and higher than the preliminary values given by Bourot-Denise et al. (2010). The mean and standard deviation are the same as those for Cr_2O_3 in olivine in Y-81020 and Colony, both usually classified as Type 3.0, though they are higher than the lowest 3.0 (Fig. 32).

The partitioning of Fe/Mg between chromite and coexisting olivine is temperature dependent (Engi, 1983; Johnson and Prinz, 1991) as well as dependent on the

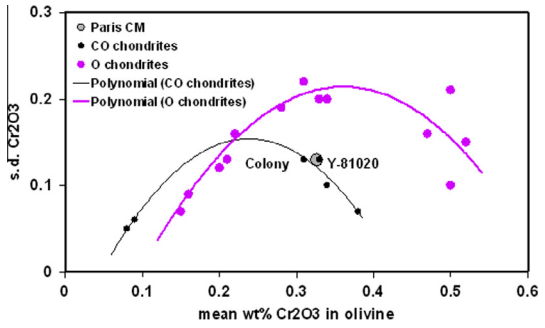

Fig. 32. Plot of the standard deviation vs. the mean of the Cr_2O_3 content of ferroan olivine, after Grossman and Brearley (2005). Paris olivine plots beside that of Colony and Y-81020, two 3.0 chondrites.

Cr/(Cr + Al) ratio of the chromite. We used the graphical approach of Johnson and Prinz (1991) to determine olivine–chromite equilibration temperatures (Hewins et al., 2011). The olivine–chromite assemblage in all chondrules in Paris plots near or above the 1400 °C isotherm, as it does for all CM chondrites (our data; Johnson and Prinz, 1991). In contrast, mildly reheated (3.1–3.3) CO chondrite olivine–chromite pairs have their K_DFe/Mg partially reset, yielding a temperature range of ~1400–600 °C (Johnson and Prinz, 1991). Thus the olivine in Paris resembles that in 3.0 chondrites, in that there has been no visible diffusion of cations due to reheating. Semarkona contains phyllosilicates in its matrix, yet is classified as an LL3.0. The water content was low however, because its matrix abundance is low and chondrule glass is preserved. The total abundance of secondary minerals in Paris is consistent with classification as a Type 2 chondrite.

6.2.2. Sulfide and metal

Hexagonal pyrrhotite contains granular pentlandite around its borders (Fig. 9a and b). Such Hpo-Pn grains correspond to category A CM chondrite sulfides (unheated group, secondary heating $T < 100$ °C) in the terminology of Kimura et al. (2011). Metal in Type I chondrules and in isolated globules in matrix is kamacite (with only very rare more Ni-rich exceptions). The range of Ni and Co (Fig. 25a) corresponds to that of metal of Group A CM chondrites (Kimura et al., 2011), rather than the more equilibrated Group B.

Inclusions of silica (Fig. 9d), daubréelite, Cr phosphide, chromite, schreibersite and troilite occur in metal (Bourot-Denise et al., 2010) often with several of these phases associated, whereas in OC and Renazzo such phases tend not to occur together (Zanda et al., 1994). There is, however, a tendency for a given kamacite globule to contain one dominant kind of precipitate, presumably related to the initial concentrations of the minor elements. Zanda et al. (1994) distinguished two generations of inclusions in metal, those formed during slow chondrule cooling and those formed during metamorphism. For Renazzo and Semarkona, inclusions were interpreted as experiencing only a very mild reheating, The secondary mineral assemblages of CM chondrites suggest low temperatures (<100 °C) and we have seen no indication in sulfides or other silicates of reheating. Thus the inclusions in metal may here have formed by exsolution during slow chondrule cooling.

7. CONCLUSIONS

(1) Paris is classified as a CM2 chondrite, based on the petrography with chondrules in a matrix containing hydrated minerals, with confirmation from mineral compositions, major and trace element abundances, O and Cr isotope systematics, magnetic properties and noble gas data. It contains less matrix than other CM chondrites, 47%, with 8% fine-grained rims and 45% chondrules. It shows very fresh and more altered domains.

(2) Eleven analyses of Paris show a wide range of oxygen isotopic compositions, with less altered material plotting closer to CO chondrites than other CM chondrites, reflecting the two component mix between ^{16}O-enriched anhydrous silicates and ^{16}O-depleted hydrated phases. The regression line for Paris data intersects the CO3 field showing that the CM and CO groups are genetically related.

(3) The Cr isotopic data of the minerals fall on a line with a slope of $^{53}Mn/^{55}Mn = (5.76 \pm 0.76) \times 10^{-6}$ with an initial $^{53}Cr_i = -0.132 \pm 0.055$. If this provides direct chronological information, the corresponding age for the Paris components, particularly Type I and Type II chondrules, corresponds to 4566.44 ± 0.66 Myr, which is close to the age of CAI and puts new constraints on the early evolution of the solar system.

(4) The REE pattern in Paris is extremely flat and resembles those of most other CM chondrite falls, especially Murchison. Paris shares the depletion pattern of elements more volatile than Mg, with high Na relative to K as in fresh CM falls. The LA-ICP-MS analysis for altered matrix exhibits the CM volatile-depleted pattern but that for unaltered matrix has undepleted abundances like CI chondrite.

(5) Paris contains large amounts of light noble gases with ^{4}He and ^{20}Ne concentrations higher than 1×10^{-4} - $cm^3\,g^{-1}$ and $1 \times 10^{-7}\,cm^3\,g^{-1}$, respectively, explained by the occurrence of a solar wind component. The Q component is also present in Paris. The ^3He_c ages are 2.81 ± 0.41 and 2.75 ± 0.18 Ma for two samples, in good agreement with the $^{21}Ne_c$ ages of 3.65 ± 0.10 and 3.55 ± 0.08 Ma.

(6) There are gradational contacts between the freshest areas with approximately 3% metal and the more PCP-rich areas. More altered matrix domains contain 1–3% calcite. Magnetite spherules are present in very restricted domains. Isolated polycrystalline Fe–Ni sulfide grains consist of pyrrhotite rimmed with pentlandite in a peripheral corona. Metal in matrix, sometimes with silica inclusions, shows thin rims of tochilinite in the freshest zones, but is extensively replaced in the more altered regions.

(7) TEM images of the matrix reveal a complex fine-grained assemblage dominated by an amorphous phase, with a gradation to a coarse-grained fibrous

morphology compatible with a serpentine structure. FIB samples also contain elongated grains of cronstedtite sometimes with fine interstratified tochilinite. Cronstedtite and fibrous material are coarser in the matrix of more altered zones. Tochilinite seen in TEM is mainly a sulfur-rich fibrous phase, locally associated with an iron oxide phase, probably magnetite. Rounded forsterite and enstatite, micron to sub-micron in size, and hollow carbon globules are observed in matrix.

(8) Serpentine and cronstedtite compositions (EMPA) run from about $Chrysotile_{60}$–$Greenalite_{40}$ to about $Chrysotile_{20}$–$Cronstedtite_{80}$ but 'serpentine' must a mixture of the amorphous phase with phyllosilicates. Compositions (ATEM) of the abundant amorphous phase and the finest fibers are comparable to the serpentine, but more Si-rich. With ATEM, S is detectable in fibrous phyllosilicates though sulfide grains are not present. Platy cronstedtite is sometimes interstratified with thin layers of tochilinite. With EPMA, some PCP includes magnetite as well as cronstedtite and tochilinite.

(9) Magnetic susceptibility measurements show the Verwey transition and a Curie temperature indicating the presence of magnetite, except for the sample that was specifically sampled in the less aqueously altered lithology of the meteorite. The average saturation magnetization (M_S) of 5.9 Am^2/kg for Paris indicates a maximum magnetite content of 6.4 wt.%, and a maximum metal content of 2.7 wt.%.

(10) The CAI are mainly fine-grained spinel-rich inclusions, with a condensation sequence of hibonite, perovskite, grossite, spinel, gehlenite, anorthite, diopside/fassaite and forsterite. Hibonite-rich CAI and melilite-rich CAI are present. RMN, with similar compositions to those in Murchison, occur exclusively inside CAI or attached to disrupted CAI minerals. The most refractory alloys occur in hibonite, with compositions dominated by Os and Ir; those in perovskite + Al-spinel CAI are Os–Ir–Mo–Ru alloys; those hosted in spinel are enriched in Pt and Rh.

(11) Type I chondrules contain olivine and pyroxene are $Fa_{0.9\pm0.7}$ and $Fs_{2.3\pm1.7}Wo_{1.4\pm1.3}$. Ca decreases and Cr increases sharply in olivine going from Fa_0 to Fa_1. Metal-rich chondrules are abundant, with a small range of Ni contents in metal, mostly ~4 to ~8 wt.%. Inclusions of silica, daubréelite, Cr phosphide, chromite, schreibersite and troilite were also observed in metal. There is a correlation of Fa vs. "Cr_2O_3" in the most forsteritic olivine ($Fa_{0.2\ to\ \sim1}$) and a negative correlation between Cr in metal and Cr_2O_3. Cr concentrations in metal are depleted relative to Ni partly due to oxidation.

(12) Type II chondrules present are IIA (PO, BO), IIAB and IIB, but also II(A)B, with minor highly ferroan olivine, and IIA(C) with augite as the only pyroxene. The range of melt-grown olivine compositions is Fa_7 to Fa_{76} and of orthopyroxene $En_{34–63}$. Type II chondrule olivine in Paris has an FeO–MnO ratio of ~100, typical of CM and CO chondrites but there exist distinct outliers from this distribution.

(13) The least altered areas contain abundant amorphous material and poorly crystalline phyllosilicates and have a microstructure like those of primitive chondrites of type 3.00. They contain up to 3x the metal content of the least altered of the classic CM chondrites. Their metal has thin tochilinite rims, corresponding to stage 1 of metal. Using an exponential fit to the PCP Index (Rubin et al., 2007) we obtained a value of 2.9 ± 0.1. This approach did not indicate that the freshest material was less altered. Cronstedtite and tochilinite were being formed in the more altered regions of Paris whereas in normal CM chondrites they were being transformed to serpentine. Aqueous alteration in Paris transported elements out of high temperature material into altered matrix, changing its composition from CI-like to CM-like.

(14) The 4.5‰ difference in $\delta^{18}O$ between the least and most altered portions can be explained by local-scale differences in the extent of alteration reflecting variation in fluid rock ratios.

(15) The mean and standard deviation of Cr_2O_3 concentrations in Paris olivine are the same as those for Cr_2O_3 in olivine in Y-81020 and Colony, both usually classified as Type 3.0. The partitioning of Fe/Mg between chromite and coexisting olivine is not reset from chondrule temperatures. Exsolution of inclusions in metal may be due to slow chondrule cooling or a very mild reheating. Pyrrhotite–pentlandite textures and compositions of Fe–Ni metal indicate unheated group A of CM chondrites.

(16) Paris is an essentially unmetamorphosed CM chondrite and it is partially altered. It is conceivably a CM2.9, though we have no systematic way to index low degrees of alteration and the alteration is heterogeneous.

ACKNOWLEDGEMENTS

We thank Michel Fialin and Frédéric Couffignal for invaluable assistance with electron probe analysis, Omar Boudouma for SEM cartography, David Troadec for the FIB sections, prepared at IEMN, University Lille 1, and Laurette Piani for help with image analysis. We are indebted to A. Elmaleh, E. Palmer and M. Zolensky for discussion. We thank the Agence Nationale de la Recherche for grants ANR-09-BLAN-436 0042 (C.C. and J.G.), and ANR-08-Blan-0260-CSD6 (C.G.) We thank the PNP (programme national de planétologie) for support of the ATEM work (H.L.), and NASA for grant NNX10AI37G (M.H.) in support of laser ablation measurements. We thank STFC for grant ST/I001964/1 (R.C.G. and I.A.F.) in support of oxygen isotope laser fluorination work. Drs. N. Abreu and W. Fujiya, and A. Krot, are thanked for detailed constructive reviews and editorial comments, respectively, which led to major improvements to the paper.

REFERENCES

Amelin Y. (2008) U–Pb ages of angrites. *Geochim. Cosmochim. Acta* **72**, 221–232.

Abreu N. M. and Brearley A. J. (2010) Early solar system processes recorded in the matrices of two highly pristine CR3 carbona-

ceous chondrites, MET 00426 and QUE 99177. *Geochim. Cosmochim. Acta* **74**, 1146–1171.

Barrat J.-A., Zanda B., Moynier F., Bollinger C., Liorzou C. and Bayon G. (2012) Geochemistry of CI chondrites: major and trace elements, and Cu and Zn isotopes. *Geochim. Cosmochim. Acta* **83**, 79–92.

Berg T., Maul J., Schönhense G., Marosits E., Hoppe P., Ott U. and Palme H. (2009) Direct evidence for condensation in the early solar system and implications for nebular cooling rates. *Astrophys. J.* **702**, L172–L176.

Berlin J., Jones R. H. and Brearley A. J. (2011) Fe–Mn systematics of type IIA chondrules in unequilibrated CO, CR, and ordinary chondrites. *Meteor. Planet. Sci.* **45**, 513–533.

Blanchard I., Gounelle M., Bourot-Denise M. and Kearsley A. (2011) Secondary processes within the Paris CM chondrite. *Meteor. Planet. Sci.* **46**, #5322 (abstr.).

Blander M., Fuchs L. H., Hurowitz C. and Land R. (1980) Primordial refractory metal particles in the Allende meteorite. *Geochim. Cosmochim. Acta* **44**, 217–223.

Bourot-Denise M., Zanda B., Marrocchi Y., Greenwood R. C., Pont S., Hewins R. H., Franchi I. A. and Cornen G. (2010) Paris: the slightly altered, slightly metamorphosed CM that bridges the gap between CMs and COs. *Lunar Planet. Sci. XLI*. Lunar Planet. Inst., Houston. #1683 (abstr.).

Brearley A. J. (1993) Matrix and fine-grained rims in the unequilibrated CO3 chondrite, ALHA77307: origins and evidence for diverse, primitive nebular dust components. *Geochim. Cosmochim. Acta* **57**, 1521–1550.

Brearley A. J. (2006) The role of microchemical environments in the alteration of CM carbonaceous chondrites. *Lunar Planet. Sci. XLI*. Lunar Planet. Inst., Houston. #2074 (abstr.).

Brennecka G. A. and Wadwha M. (2012) Uranium isotope compositions of the basaltic angrite meteorites and the chronological implications for the early solar system. *Proc. Nat. Acad. Sci. U. S. A* **109**, 9299–9303.

Browning L. B., McSween, Jr., H. Y. and Zolensky M. E. (1996) Correlated alteration effects in CM carbonaceous chondrites. *Geochim. Cosmochim. Acta* **60**, 2621–2633.

Busemann H., Baur H. and Wieler R. (2000) Primordial noble gases in "phase Q" in carbonaceous and ordinary chondrites studied by closed system etching. *Meteor. Planet. Sci.* **35**, 949–973.

Caillet Komorowski C., Boudouma O., Reynard B., Van de Moortèle B. and El Goresy A. (2011) Insights on the thermal history of the Paris CM chondrite based on the phase relations of its opaque assemblages. *Meteor. Planet. Sci.* **45**, A35, #5289 (abstr.).

Chizmadia L. J. and Brearley A. J. (2008) Mineralogy, aqueous alteration, and primitive textural characteristics of fine-grained rims in the Y-791198 CM2 carbonaceous chondrite: TEM observations and comparison to ALHA81002. *Geochim. Cosmochim. Acta* **72**, 602–625.

Clayton R. N. and Mayeda T. K. (1984) The oxygen isotope record in Murchison and other carbonaceous chondrites. *Earth Planet. Sci. Lett.* **67**, 151–166.

Clayton R. N. and Mayeda T. K. (1999) Oxygen isotope studies of carbonaceous chondrites. *Geochim. Cosmochim. Acta* **63**, 2089–2104.

Connelly J. N., Bizzarro M., Krot A. N., Nordlund A., Wielandt D. and Ivanova M. A. (2012) The absolute chronology and thermal processing of solids in the solar protoplanetary disk. *Science* **338**, 651–655.

Consolmagno G. J., Britt D. J. and Macke R. J. (2008) The significance of meteorite density and porosity. *Chemie der Erde* **68**, 1–29.

Croat T. K., Berg T., Bernatowicz T., Groopman E. and Jhadav M. (2013) Refractory metal nuggets within presolar graphite: first condensates from acircumstellar environment. *Meteor. Planet. Sci.* **48**, 686–699.

Dunlop D. J. and Özdemir Ö. (1997) *Rock Magnetism: fundamentals and Frontiers*. Cambridge Univ. Press, Cambridge.

Elmaleh A., Tarantino S. C., Zema M., Zanda B., Devouard B. and Fialin M. (2011) Low-T magnetic properties of 5 CM2 chondrites: comparison with the signature of cronstedtite and with preliminary results from the Paris chondrite. *Meteor. Planet. Sci.* **45**, #5492 (abstr.).

Elmaleh A., Tarantino S. C., Zema M., Devouard B. and Fialin M. (2012) The low-temperature magnetic signature of Fe-rich serpentine in CM2 chondrites, comparison with terrestrial cronstedtite and evolution with the degree of alteration. *Geochem. Geophys. Geosyst.* **13**, Q05Z42.

Engi M. (1983) Equilibria involving Al–Cr spinel: I. Mg–Fe exchange with olivine. Experiments, thermodynamic analysis, and consequences for geothermometry. *Amer. J. Sci.* **283A**, 29–71.

Eugster O. and Michel Th. (1995) Commo asteroid break-up events of eucrites, diogenites, and howardites and cosmic-ray production rates for noble gases in achondrites. *Geochim. Cosmochim. Acta* **59**, 177–199.

Eugster O., Herzog G. F., Marti K. and Caffee M. W. (2006) Irradiation records, cosmic-ray exposure ages, and transfer times of meteorites. In *Meteorites and the early solar system II* (eds. D. S. Lauretta and , Jr.H. Y. McSween). Arizona, The University of Arizona, Tucson, pp. 829–851.

Eugster O., Lorenzetti S., Krähenbühl U. and Marti K. (2007) Comparison of cosmic-ray exposure ages and trapped noble gases in chondrule and matrix samples of ordinary, enstatite, and carbonaceous chondrites. *Meteor. Planet. Sci.* **42**, 1351–1371.

Frank D. R., Zolensky M. E. and Le L. (2012) Using the Fe/Mn ratio of FeO-rich olivine in Wild 2, chondrite matrix, and type IIA chondrules to disentagle their histories. *Lunar Planet. Sci. XLIII*. Lunar Planet. Inst., Houston. #2748 (abstr.).

Friedrich J. M., Wang M.-S. and Lipschutz M. E. (2002) Comparison of the trace element composition of Tagish Lake with other primitive carbonaceous chondrites *Meteor. Planet. Sci.* **37**, 677–686.

Fujiya W., Sugiura N., Sano Y. and Hiyagon H. (2013) Mn–Cr ages of dolomites in CI chondrites and the Tagish Lake ungrouped carbonaceous chondrite. *Earth Planet. Sci. Lett.* **362**, 130–142.

Gaboardi M. and Humayun M. (2009) Elemental fractionation during LA-ICP-MS analysis of silicate glasses: implications for matrix-independent standardization. *J. Anal. At. Spectrom.* **24**, 1188–1197. http://dx.doi.org/10.1039/b900876d.

Glavin D. P., Kubny A., Jagoutz E. and Lugmair G. W. (2004) Mn–Cr isotope systematics of the D'Orbigny angrite. *Meteor. Planet. Sci.* **39**, 693–700.

Göpel C., Birck J.-L. and Zanda B. (2011) Mn/Cr systematics in carbonaceous chondrites: mineral isochrons versus stepwise dissolution. *Min. Mag.* **75**, 936.

Göpel C., Birck J.-L., Cartigny P., Assayag N. and Zanda B. (2012) ^{54}Cr and ^{17}O in carbonaceous chondrites and an old ^{53}Cr/^{53}Mn age of the Paris meteorite. *Min. Mag.* **76**, 1775.

Göpel C., Birck J. -L., Cartigny P., Assayag N. and Zanda B. (2013) ^{54}Cr and (Δ^{17}O in carbonaceous chondrites and an old ^{53}Cr/^{53}Mn age for the Paris meteorite (submitted for publication).

Greenwood R. C. and Franchi I. A. (2004) Alteration and metamorphism of CO3 chondrites: evidence from oxygen and carbon isotopes. *Meteor. Planet. Sci.* **39**, 1823–1838.

Greenwood R. C., Franchi I. A., Gibson J. M. and Benedix G. K. (2012) Oxygen isotope variation in primitive achondrites: the influence of primordial, asteroidal and terrestrial processes. *Geochim. Cosmochim. Acta* **94**, 146–163.

Greshake A. (1997) The primitive matrix components of the unique carbonaceous chondrite ACFER 094: a TEM study. *Geochim. Cosmochim. Acta* **61**, 437–452.

Grossman J. N. and Zipfel J. (2001). *Meteor. Planet. Sci.* **36**, A293–A322.

Grossman J. N. and Brearley A. J. (2005) The onset of metamorphism in ordinary and carbonaceous chondrites. *Meteor. Planet. Sci.* **40**, 87–122.

Grossman L. and Olsen E. (1974) Origin of the high-temperature fraction of C2 chondrites. *Geochim. Cosmochim. Acta* **38**, 173–187.

Haack H., Grau T., Bischoff A., Horstmann M., Wasson J., Sørensen A. N., Laubenstein M., Ott U., Palme H., Gellissen M., Greenwood R. C., Pearson V. K., Franchi I. A., Gabelica Z. and Schmitt-Kopplin P. (2012) Maribo – a new CM fall from Denmark. *Meteor. Planet. Sci.* **47**, 30–50.

Harries D., Berg T., Langenhorst F. and Palme H. (2012) Structural clues to the origin of refractory metal alloys as condensates of the solar nebula. *Meteor Planet. Sci.* **47**, 2148–2159.

Heber V., Wieler R., Baur H., Olinger C., Friedmann T. A. and Burnett D. S. (2009) Noble gas composition of the solar wind as collected by the Genesis mission. *Geochim. Cosmochim. Acta* **73**, 7414–7432.

Hewins R. H. and Zanda B. (2011) Type II chondrule origin in O and C chondrites. *Meteor. Planet. Sci.* **45**, A94, #5144 (abstr.).

Hewins R. H. and Zanda B. (2012) Origin of FeO–MnO olivine reservoirs in chondrules. *Meteor. Planet. Sci.* **46**, #5274 (abstr.).

Hewins R. H., Zanda B. and Bourot-Denise M. (2011) The formation of type II chondrules in CM chondrites: the view from Paris. *Lunar Planet. Sci. XLII*. Lunar Planet. Inst., Houston. #1914 (abstr.).

Humayun M. (2012) Chondrule cooling rates inferred from diffusive profiles in metal lumps from the Acfer 097 CR2 chondrite. *Meteor. Planet. Sci.* **47**, 1191–1208.

Humayun M., Simon S. B. and Grossman L. (2007) Tungsten and hafnium distribution in calcium-aluminum inclusions CAIs from Allende and Efremovka. *Geochim. Cosmochim. Acta* **71**, 4609–4627.

Humayun M., Davis F. A. and Hirschmann M. M. (2010) Major element analysis of natural silicates by laser ablation ICP-MS. *J. Anal. At. Spectrom.* **25**, 998–1005. http://dx.doi.org/10.1039/C001391A.

Humbert F., Libourel G., France-Lanord C., Zimmermann L. and Marty B. (2000) CO_2-laser extraction-static mass spectrometry analysis of ultra-low concentrations of nitrogen in silicates. *Geostand. Newsl.* **24**, 255–260.

Jarosewich E. (1990) Chemical analyses of meteorites: a compilation of stony and iron meteorite analyses. *Meteoritics* **25**, 323–337.

Johnson C. and Prinz M. (1991) Chromite and olivine in type II chondrules in carbonaceous and ordinary chondrites: implications for thermal histories and group differences. *Geochim. Cosmochim. Acta* **55**, 893–904.

Kallemeyn G. W. and Wasson J. T. (1981) The compositional classification of chondrites- I. The carbonaceous chondrite groups. *Geochim. Cosmochim. Acta* **45**, 1217–1230.

Kallemeyn G. W., Rubin A. E. and Wasson J. T. (1994) The compositional classification of chondrites: VI. The CR carbonaceous chondrite group. *Geochim. Cosmochim. Acta* **58**, 2873–2888.

Keller L. P. and Messenger S. (2012) Formation and processing of amorphous silicates in primitive carbonaceous chondrites and cometary dust. *Lunar Planet. Sci. XLIII*. Lunar Planet. Inst., Houston. #1880 (abstr.).

Kimura M., Grossman J. N. and Weisberg M. K. (2011) Fe–Ni metal and sulfide minerals in CM chondrites, an indicator for thermal history. *Meteor. Planet. Sci.* **46**, 431–442.

Kita N. T. and Ushikubo T. (2012) Evolution of protoplanetary disk inferred from ^{26}Al chronology of individual chondrules. *Meteor. Planet. Sci.* **47**, 1108–1119.

Kring D. A. (1986) The petrology of meteoritic chondrules: evidence for fluctuating conditions In the solar nebula. Ph. D. thesis, Harvard Univ., p. 346.

Lauretta D. S., Hua X. and Buseck P. R. (2000) Mineralogy of fine-grained rims in the ALH 81002 CM chondrite. *Geochim. Cosmochim. Acta* **64**, 3263–3273.

Leroux H., Rietmeijer F. J. M., Velbel M. A., Brearley A. J., Jacob D., Langenhorst F., Bridges J. C., Zega T. J., Stroud R. M., Cordier P., Harvey R. P., Lee M., Gounelle M. and Zolensky M. E. (2008) A TEM study of thermally modified Comet 81P/Wild 2 dust particles by interactions with the aerogel matrix during the Stardust capture process. *Meteor. Planet. Sci.* **43**, 97–120.

Leroux H., Cuvillier P., Zanda B. and Hewins R. H. (2013) A TEM investigation of the fine-grained matrix of the Paris CM chondrite. *Lunar Planet. Sci. XLIV*. Lunar Planet. Inst., Houston. #1528 (abstr.).

Liu M.-C., Chaussidon M., Göpel C. and Lee T. (2012) A heterogeneous solar nebula as sampled by CM hibonite grains. *Earth Planet. Sci. Lett.* **327**, 75–83.

Marrocchi Y., Derenne S., Marty B. and Robert F. (2005) Interlayer trapping of noble gases in insoluble organic matter of primitive meteorites. *Earth Planet. Sci. Lett.* **236**, 569–578.

Marrocchi Y., Marty B., Reinhardt P. and Robert F. (2011) Adsorption of xenon ions onto defects in organic surfaces: implications for the origin and the nature of organics in primitive meteorites. *Geochim. Cosmochim. Acta* **75**, 6255–6266.

Marty B., Kelley S. and Turner G. (2010) Chronology and shock history of the Bencubbin meteorite: a nitrogen, noble gas, and Ar–Ar investigation of silicates, metal and fluid inclusions. *Geochim. Cosmochim. Acta* **74**, 6636–6653.

McSween, Jr., H. Y. (1977) Chemical and petrographic constraints on the origin of chondrules and inclusions in carbonaceous chondrites. *Geochim. Cosmochim. Acta* **41**, 1843–1860.

McSween, Jr., H. Y. (1979) Alteration in CM carbonaceous chondrites inferred from modal and chemical variations in matrix. *Geochim. Cosmochim. Acta* **43**, 1761–1770.

Menyeh A. and O'Reilly W. (1991) The magnetization process in monoclinic pyrrhotite (Fe7S8) particles containing few domains. *Geophys. J. Int.* **104**, 387–399.

Merouane S., Djouadi Z., Le Sergeant d'Hendecourt L., Zanda B. and Borg J. (2012) Hydrocarbon materials of likely interstellar origin from the Paris meteorite. *Astrophys. J.* **756**, 154.

Metzler K., Bischoff A. and Stöffler D. (1992) Accretionary dust mantles in CM chondrites: evidence for solar nebula processes. *Geochim. Cosmochim. Acta* **56**, 2873–2897.

Miller M. F., Franchi I. F., Sexton A. S. and Pillinger C. T. (1999) High precision $d^{17}O$ isotope measurements of oxygen from silicates and other oxides: methods and applications. *Rapid Commun. Mass Spectrom.* **13**, 1211–1217.

Mittlefehldt D. W. and Wetherill G. W. (1979) Rb–Sr studies of CI and CM chondrites. *Geochim. Cosmochim. Acta* **43**, 201–206.

Mostefaoui S. (2011) The search for presolar oxides in Paris. *Meteor. Planet. Sci.* **45**, A94, #5170 (abstr.).

Nakamura N. (1974) Determination of REE, Ba, Fe, Mg, Na and K in carbonaceous and ordinary chondrites. *Geochim. Cosmochim. Acta* **38**, 757–775.

Nakamura T. (2005) Post-hydration thermal metamorphism of carbonaceous chondrites. *J. Mineral. Petrol. Sci.* **100**, 260–272.

Nazarov M. A., Kurat G., Brandstaetter F., Ntaflos T., Chaussidon M. and Hoppe P. (2009) Phosphorus-bearing sulfides and their associations in CM chondrites. *Petrology* **17**, 101–123.

Ozima M. and Podosek F. A. (2002) *Noble Gas Geochemistry*. Cambridge Univ. Press, Cambridge, p. 286.

Palme H. and Wlotzka F. (1976) A metal particle from a Ca, Al rich inclusion from the meteorite Allende, and the condensation of refractory siderophile elements. *Earth Planet. Sci. Lett.* **33**, 45–60.

Palme H., Hutcheon I. D. and Spettel B. (1994) Composition and origin of refractory-metal-rich assemblages in a Ca, Al-rich Allende inclusion. *Geochim. Cosmochim. Acta* **58**, 495–513.

Palmer E. E. (2009) Volatiles on solar system objects: carbon dioxide on Iapetus and aqueous alteration in CM chondrites. Ph. D. thesis, Arizona Univ., p. 234.

Palmer E. E. and Lauretta D. S. (2011) Aqueous alteration of kamacite in CM chondrites. *Meteor. Planet. Sci.* **46**, 1587–1607.

Remusat L., Bernard S., Le Guillou C. and Brearley A. (2011) Parent body influence on organic matter: the message from Paris. *Meteor. Planet. Sci.* **45**, #5327 (abstr.).

Rochette P., Gattacceca J., Bonal L., Bourot-Denise M., Chevrier V., Clerc J.-P., Consolmagno G., Folco L., Gounelle M., Kohout T., Pesonen L., Quirico E., Sagnotti L. and Skripnik A. (2008) Magnetic classification of stony meteorites: 2. Non-ordinary chondrites. *Meteor. Planet. Sci.* **43**, 959–980.

Rubin A. E. and Wasson J. T. (1987) Chondrules, matrix and coarse-grained chondrule rims in the Allende meteorite: origin, interrelationships and possible precursor components. *Geochim. Cosmochim. Acta* **51**, 1923–1937.

Rubin A. E., Trigo-Rodrıguez J. M., Huber H. and Wasson J. T. (2007) Progressive aqueous alteration of CM carbonaceous chondrites. *Geochim. Cosmochim. Acta* **71**, 2361–2382.

Russell S. D. J., Longstaffe F. J., King P. L. and Larson T. E. (2010) The oxygen-isotope composition of chondrules and isolated forsterite and olivine grains from the Tagish Lake carbonaceous chondrite. *Geochim. Cosmochim. Acta* **74**, 2484–2499.

Scherer P. and Schultz L. (2000) Noble gas record, collisional history, and paring of CV CO., CK, and other carbonaceous chondrites. *Meteor. Planet. Sci.* **35**, 145–153.

Schulze H. (2007) Mineralogy and mineral chemistry of noble metal grains in R chondrites. *Lunar Planet. Sci. XXX*. Lunar Planet. Inst., Houston. #1720 (abstr.).

Schwander D., Berg T., Ott U., Schönhense G. and Palme H. (2011) Refractory metal nugetts in carbonaceous chondrites and early solar nebula condensates. *Lunar Planet. Sci.* #9070 (abstr.).

Schwander D., Berg T., Ott U., Schönhense G. and Palme H. (2012) Formation of refractory metal alloys and their occurrence in CAIs. *Meteor. Planet. Sci.* **47**, A348, #5203 (abstr.).

Schwander D., Berg T., Ott U., Schönhense G. and Palme H. (2013) Clues to formation of refractory metal nuggets. *Lunar Planet. Sci. XLIV*. Lunar Planet. Inst., Houston. #1959 (abstr.).

Simon S. B. and Grossman L. (2003) Petrography and mineral chemistry of the anhydrous component of the Tagish Lake carbonaceous chondrite. *Meteor. Planet. Sci.* **38**, 813–825.

Simon S., Grossman L., Hutcheon I., Phinney D., Weber P. and Fallon S. (2006) Formation of spinel-, hibonite-rich inclusions found in CM2 carbonaceous chondrites. *Am Mineral* **91**, 1675–1687.

Tatsumoto M., Unruh D. M. and Desborough G. A. (1976) U–Th–Pb and Rb–Sr systematics of Allende and U–Th–Pb systematics of Orgueil. *Geochim. Cosmochim. Acta* **40**, 617–634.

Tomeoka K. and Buseck P. R. (1985) Indicators of aqueous alteration in CM carbonaceous chondrites: microtextures of a layered mineral containing Fe, S, O and Ni. *Geochim. Cosmochim. Acta* **49**, 2149–2163.

Trinquier A., Birck J.-L. and Allègre C.-J. (2007) Widespread ^{54}Cr heterogeneity in the inner solar system. *Astrophys. J.* **655**, 1179–1185.

Wasson J. T. and Kallemeyn G. W. (1988) Composition of chondrites. *Philos. Trans.* **325**, 535–544.

Wieler R. and Baur H. (1994) Krypton and xenon from the solar wind and solar energetic particles in two lunar ilmenites of different antiquity. *Meteoritics* **29**, 570–580.

Wolf D. and Palme H. (2001) The solar system abundances of phosphorus and titanium and the nebular volatility of phosphorus. *Meteor. Planet. Sci.* **36**, 559–571.

Wolf R., Richter G., Woodrow A. and Anders E. (1980) Chemical fractionations in meteorites. XI–C2 chondrites. *Geochim. Cosmochim. Acta* **44**, 711–717.

Yin Q.-Z., Jacobsen B., Moynier F. and Hutcheon I. D. (2007) ^{53}Mn–^{53}Cr chronometry for chondrules. *Astrophys. J.* **662**, L43–L46.

Yin Q. -Z., Yamashita K., Yamakawa A., Tanaka R., Jacobsen B., Ebel D., Hutcheon I. D. and Nakamura E. (2009) ^{53}Mn–^{53}Cr systematics of allende chondrules and epsilon ^{54}Cr–Δ^{17}O correlation in bulk carbonaceous chondrites. *Lunar Planet. Sci. XL*. Lunar Planet. Inst., Houston. #2006 (abstr.).

Zanda B., Bourot-Denise M., Perron C. and Hewins R. H. (1994) Origin and metamorphic redistribution of silicon, chromium and phosphorus in the metal of chondrites. *Science* **265**, 1846–1849.

Zanda B., Bourot-Denise M., Hewins R. H., Barrat J.-A. and Gattacceca J. (2010) The Paris CM chondrite yields new insights on the onset of parent body alteration. *Meteor. Planet. Sci.* **44**, A222, #5312 (abstr.).

Zanda B., Humayun M., Barrat J. -A., Bourot-Denise M. and Hewins R. H. (2011a) Bulk and matrix composition of Paris. Inferences on parent-body alteration and the origin of matrix-chondrule complementarity. *Lunar Planet. Sci. XLII*. Lunar Planet. Inst., Houston. #2040 (abstr.).

Zanda B., Humayun M., Barrat J.-A., Bourot-Denise M. and Hewins R. H. (2011b) Chemistry of carbonaceous chondrite matrices: parent-body alteration and chondrule-matrix complementarity. *Meteor. Planet. Sci.* **45**, #5358 (abstr.).

Zega T. J., Nittler L. R., Busemann H., Hoppe P. and Stroud R. M. (2007) Coordinated isotopic and mineralogic analyses of planetary materials enabled by in situ lift-out with a focused ion beam scanning electron microscope. *Meteor. Planet. Sci.* **42**, 1373–1386.

Zolensky M., Barrett R. and Browning L. (1993) Mineralogy and composition of matrix and chondrule rims in carbonaceous chondrites. *Geochim. Cosmochim. Acta* **57**, 3123–3148.

Associate editor: Alexander N. Krot